Ocean Modelling 152 (2020) 101656

Contents lists available at ScienceDirect

Ocean Modelling

journal homepage: www.elsevier.com/locate/ocemod

On the interplay between horizontal resolution and wave drag and their effect on tidal baroclinic mode waves in realistic global ocean simulations

Maarten C. Buijsman [a,*], Gordon R. Stephenson [a], Joseph K. Ansong [b], Brian K. Arbic [c], J.A. Mattias Green [d], James G. Richman [e], Jay F. Shriver [f], Clément Vic [g], Alan J. Wallcraft [e], Zhongxiang Zhao [h]

[a] School of Ocean Science and Engineering, University of Southern Mississippi, Stennis Space Center, MS, USA
[b] Department of Mathematics, University of Ghana, Accra, Ghana
[c] Earth and Environmental Sciences, University of Michigan, Ann Arbor, MI, USA
[d] School of Ocean Sciences, Bangor University, Menai Bridge, Anglesey, UK
[e] Center for Ocean-Atmospheric Prediction Studies, Florida State University, Tallahassee, FL, USA
[f] Naval Research Laboratory, Stennis Space Center, MS, USA
[g] University of Brest, CNRS, IRD, Ifremer, Laboratoire d'Océanographie Physique et Spatiale, Plouzané, Bretagne, France
[h] Applied Physics Laboratory, University of Washington, Seattle, WA, USA

ARTICLE INFO

Keywords:
Numerical models
Internal tides
Wave damping
Vertical modes

ABSTRACT

The effects of horizontal resolution and wave drag damping on the semidiurnal M_2 tidal energetics are studied for two realistically-forced global HYbrid Coordinate Ocean Model (HYCOM) simulations with 41 layers and horizontal resolutions of 8 km (1/12.5°; H12) and 4 km (1/25°; H25). In both simulations, the surface tidal error is minimized by tuning the strength of the linear wave drag, which is a parameterization of the surface-tide energy conversion to the unresolved baroclinic wave modes. In both simulations the M_2 surface tide error with TPXO8-atlas, an altimetry constrained model, is 2.6 cm. Compared to H12, the surface tide energy conversion to the resolved vertical modes is increased by 50% in H25. This coincides with an equivalent reduction in the tuned loss of energy from the surface tide to the wave drag. For the configurations studied here, the horizontal and not the vertical resolution is the factor limiting the number of vertical modes that are resolved in most of the global ocean: modes 1–2 in H12 and modes 1–5 in H25. The wave drag also dampens the resolved internal tides. The 40% reduction in wave-drag strength does not result in a proportional increase in the mode-1 energy density in H25. In the higher-resolution simulations, topographic mode-scattering and wave–wave interactions are better resolved. This allows for an energy flux out of mode 1 to the higher modes, mitigating the need for an internal tide damping term. The HYCOM simulations are validated with analytical conversion models and altimetry-inferred sea-surface height, fluxes, and surface tide dissipation. H25 agrees best with these data sets to within ~10%. To facilitate the comparison of stationary tide signals extracted from time series with different durations, we successfully apply a spatially-varying correction factor.

1. Introduction

Over the last decade or so, much progress has been made in introducing tides into ocean general circulation models. Arbic et al. (2018) detail the progress made in models of this type, including the progress in model-observational comparisons. While the barotropic tides in some models of this type are now reasonably accurate in both amplitude and phase (Ngodock et al., 2016), the accuracy of modeled internal tides, and their sensitivity to damping, is at a somewhat more nascent phase (Ansong et al., 2015; Buijsman et al., 2016; Arbic et al., 2018). Internal tides are internal waves at tidal frequencies and they are generated by the vertical displacement of isopycnals as the barotropic tide flows over rough bathymetry (Buijsman et al., 2019). We are motivated to study internal tides for several reasons. First, internal tides act to redistribute energy from the barotropic tide on a global scale. The dissipation of internal tides, whether close to their generation sites or away across ocean basins (MacKinnon et al., 2017; de Lavergne et al., 2019), contributes roughly one terawatt (TW) of energy to vertical mixing globally (Munk and Wunsch, 1998; Wunsch and Ferrari, 2004; Waterhouse et al., 2014; Kunze, 2017). A better understanding of internal wave mixing is relevant to develop better mixing parameterizations for climate models (Melet et al., 2013; MacKinnon et al., 2017). Second, low-mode internal tides can propagate for 1000s of kilometers, as observed in satellite altimetry (Ray and Zaron, 2016;

* Corresponding author.
E-mail address: maarten.buijsman@usm.edu (M.C. Buijsman).

https://doi.org/10.1016/j.ocemod.2020.101656
Received 17 December 2019; Received in revised form 19 May 2020; Accepted 21 June 2020
Available online 26 June 2020

Zhao et al., 2016), and they may affect the local generation of internal tides across ocean basins (Kelly and Nash, 2010; Buijsman et al., 2010; Ponte and Cornuelle, 2013). The inclusion of these remote internal tides as a boundary condition is relevant for the correct simulation of internal tides in regional models (Kerry et al., 2013; Mazloff et al., 2020). Finally, correctly predicting the time varying amplitudes and phases of the internal tides facilitates the separation of the (sub)mesoscale circulation from the internal tides, which is important for the upcoming Surface Water and Ocean Topography (SWOT) mission (Fu et al., 2012).

Many facets affect the predictability of the internal tide in (global) ocean models: surface tidal forcing, time variable background stratification and flow, topography, model resolution, and subgridscale dissipation parameterizations. In this paper, we analyze the M_2 internal tide energetics in state-of-the-art, realistically forced, global forward HYbrid Coordinate Ocean Model (HYCOM) simulations. In particular, we are interested in how the model horizontal resolution and wave drag damping affect the internal tide predictability.

Internal tides undergo a myriad of dissipative processes due to lee-wave breaking at generation, wave–wave interactions, topographic scattering, shear instabilities, dissipation at critical slopes, and shoaling on farfield continental shelves (for an overview, see MacKinnon et al., 2017). These processes are generally not (well) resolved in regional and global numerical ocean models and they need to be parameterized. In general, these parameterizations are relatively crude and do not differentiate between the various dissipation processes. For example, Niwa and Hibiya (2014) used a tuned linear damping term that operates on the baroclinic velocities in their global model with a damping time of 30 days. HYCOM uses a linear wave drag term that operates on both the near-bottom barotropic and baroclinic tidal velocities (Arbic et al., 2010; Shriver et al., 2012; Ansong et al., 2015; Buijsman et al., 2016). If the wave drag is not applied to the baroclinic velocities, Ansong et al. (2015) showed that the internal tides become too energetic as compared to the satellite altimetry. However, additional wave damping is not used in all global ocean model simulations. For example, the realistically forced global MITgcm (Marshall et al., 1997) is run without wave drag at 1/48° horizontal resolution and its solution is too energetic in the tidal bands when compared to observations (Savage et al., 2017a; Yu et al., 2019; Luecke et al., 2020). Müller et al. (2012) performed global simulations with the MPI-OM model (Jungclaus et al., 2006) at 1/10° horizontal resolution without wave drag, and found that the internal tides are weaker than observed, most likely because the model set up is too diffusive.

Wave drag parameterizations were originally intended for global barotropic models, which do not resolve internal tides. These schemes represent the energy conversion from the surface tide to the full spectrum of unresolved internal tides at mid-ocean ridges and continental shelves (Jayne and St. Laurent, 2001; Green and Nycander, 2013; Buijsman et al., 2015). However, these wave-drag parameterizations have also been applied in baroclinic global-ocean simulations to primarily optimize the surface-tide accuracy. Arbic et al. (2004) minimized the surface tidal error by tuning the wave drag with a drag scale in global baroclinic simulations. Baroclinic global-ocean models can only convert surface tidal energy to internal-wave modes, for which the horizontal and vertical grid spacings determine how well the motions are resolved. The energy conversion to the unresolved higher modes is parameterized by the wave drag. If one assumes that the drag scale for a drag scheme that represents the full modal spectrum is 1 in barotropic simulations, it should be <1 in baroclinic simulations, and increasingly smaller for higher (horizontal) resolutions, as more vertical modes are resolved.

It is well-known that an increase in vertical and horizontal resolution increases the wave energy, in particular that of the smaller-scale waves. In global internal-tide simulations, Niwa and Hibiya (2014) showed that the barotropic to baroclinic energy conversion increased for higher horizontal resolutions, but they did not specify if this increase was due to the contribution of higher modes. The effect of model resolution on realistically forced global baroclinic simulations has been explored in several studies. When analyzing HYCOM simulations with horizontal resolutions of 8 and 4 km and MITgcm simulations with resolutions of 8, 4, and 2 km, it was found that the higher frequency and higher wave-number tails of the energy spectra had more energy and the simulated frequency spectra were closer to observations in the higher-resolution simulations (Savage et al., 2017b,a; Luecke et al., 2020). The higher-resolution simulations featured stronger non-linear wave–wave interactions, facilitating an improved cascade to smaller scales (Müller et al., 2015; Ansong et al., 2018).

One objective of this paper is to understand the effects of both horizontal resolution and wave-drag strength on the energetics of the resolved internal tide modes in realistically forced global HYCOM simulations with horizontal grid sizes of about 8 km (1/12°) and 4 km (1/25°), and 41 hybrid layers in the vertical. In these simulations, the wave drag affects both the surface and internal tides. Our focus is on the M_2 internal tide as it contains about 70% of all tidal energy (Egbert and Ray, 2003). We analyze the internal-tide modal energy balance (Kelly et al., 2012) on a global scale, which has not been done before in HYCOM or any other global forward model. A second objective is to validate these HYCOM simulations with internal-tide sea-surface height amplitudes and modal-energy fluxes inferred from altimetry, surface-tide dissipation rates estimated from an altimetry-constrained model, and modal-conversion rates computed from analytical models. As in Ansong et al. (2015), we note that the magnitude of the altimetry-inferred sea-surface height amplitudes and the modal-energy fluxes is affected by the duration of the time series they are extracted from. Since our model simulations are shorter we apply a correction, newly developed in the present work, to facilitate a comparison. The correction factor is explained in the Appendix.

In the following sections, we first present the model set-up and energy equations. We then discuss the M_2 surface and internal tide energetics that are not decomposed into vertical modes. This is followed by a presentation of the modal energetics. In the discussion section, we synthesize our results and compare them with the literature. We end with conclusions.

2. Methodology

2.1. HYCOM

HYCOM is the operational global ocean forecast model used by the United States Navy (Metzger et al., 2014). The hybrid vertical coordinate is isopycnal in the open ocean and transitions to terrain-following in shallow water, with z-coordinates to resolve the surface mixed layer. We discuss two model simulations that are run in a forward (non-data-assimilative) mode on a tripolar grid at 1/12.5° (8 km) and 1/25° (4 km) nominal horizontal resolutions with 41 layers in the vertical (27 levels above 250 m, most 8 m apart). Hereafter, we refer to these simulations as H12 and H25, respectively. In HYCOM terminology, these simulations are also referred to as expt_06.1 and expt_22.1. Both simulations are run with realistic atmospheric forcing from the NAVY Global Environmental Model (NAVGEM) (Hogan et al., 2014) and astronomical tidal forcing for the M_2, S_2, K_1, O_1, and N_2 tidal constituents. To account for numerical errors in the tidal solution due to imperfect topography and damping terms, an Augmented State Ensemble Kalman Filter (ASEnKF) is applied to optimize the spatially varying Self Attraction and Loading (SAL) term used in the simulations (Ngodock et al., 2016). Both simulations employ a quadratic bottom drag and a linear wave drag to dampen tidal flows (Ansong et al., 2015).

To account for the energy conversion from the surface tide to the unresolved baroclinic modes and to dampen the resolved internal tides, we use the scalar internal wave drag parameterization of Jayne and St. Laurent (2001)

$$\mathbb{C} = \frac{\pi}{L_t}\hat{H}^2 N_b, \tag{1}$$

where $\hat{H}$ is the bottom roughness, N_b is the buoyancy frequency at the bottom, and L_t is the wavelength of the topography. The calculation of this wave drag and its performance in barotropic simulations is discussed in Buijsman et al. (2015). The Jayne and St. Laurent (2001) drag is applied to the total (barotropic and baroclinic) flow in the bottom 500 m for seafloor depths greater than 1000 m. In addition to tidal flows, the drag also acts on subtidal bottom flows. To compensate for this, an 'anti-drag' is applied to the bottom flows. The anti-drag uses non-tidal bottom velocities that are a weighted average over 49 h and lagged by 24 h. For a detailed description of the application of the anti-drag and its impact on the baroclinic simulations, the reader is referred to Arbic et al. (2010). To minimize the impact on non-tidal motions, we clip the value of $\mathbb{C}$ at rough topography so that its minimum e-folding time $\frac{H}{\mathbb{C}} = 1$ day, where H is seafloor depth. Moreover, $\mathbb{C}$ is set to zero for smooth topography with an e-folding time > 10 days.

For each model simulation, the wave drag is tuned with a drag scale χ to minimize the global-mean M_2 root-mean-square error ($RMSE$) between the altimetric sea-surface height from TPXO8-atlas (Egbert et al., 1994) and the simulated sea-surface height. The tuned wave-drag scale of Buijsman et al. (2015) is reset to $\chi = 1.0$ before the tuning of the H12 and H25 simulations. After tuning, the optimal drag scales in H12 and H25 are 0.5 and 0.3 respectively. This implies that the barotropic energy loss to the resolved (parameterized) internal tides in H25 has been increased (reduced) relative to H12. The $RMSE$ is 2.6 cm for both simulations, which is similar to the results in Ngodock et al. (2016).

Instead of tuning the wave drag, one could argue that it would make more sense to extract the modal drag component from the analytical modal conversion models of Falahat et al. (2014) or Vic et al. (2019). For example, if the numerical model simulation resolves modes 1 and 2, one needs to apply the wave drag components of modes 3 and higher in the numerical simulation. We have attempted this for the Falahat et al. (2014) scheme in HYCOM (unpublished results), but the high-mode drag scheme needed to be modified – through smoothing, clipping, and tuning – such that it defeated the purpose of having such scheme. Moreover, the surface and internal tides in simulations with this modal drag scheme do not significantly improve as compared to the full-spectrum Jayne and St. Laurent (2001) scheme.

The three-dimensional (3D) HYCOM output is saved hourly for one full year for H12 from October 2011 through September 2012. Due to storage limitations, we can only store 2D fields of H25, such as sea-surface height (SSH), for an entire year (1 January to 31 December 2016) at an hourly frequency. The 3D data for H25 is only stored for the month of September 2016. In this paper, we perform the energy diagnostics on model data for the first two weeks of September 2012 (H12) and September 2016 (H25). We compare sea-surface height variance computed for two-week and one-year long HYCOM time series with altimetry.

2.2. M_2 energetics

The HYCOM model output is analyzed using two different methods. First, we perform M_2 barotropic and baroclinic energetic calculations for the 3D fields that are *not* decomposed into vertical modes. In the second method, we decompose the 3D fields into vertical modes and compute M_2 energy metrics for these modes. The application of these two methods facilitates the comparison of the model results with various observational data sets and analytical models.

2.2.1. Barotropic and undecomposed baroclinic energetics

To better frame the modal energetics, we first consider the barotropic and undecomposed baroclinic energy balances for the M_2 tide as in Buijsman et al. (2016). The time-averaged depth-integrated barotropic energy balance reads

$$P_0 = \nabla \cdot \mathbf{F}_0 + C_L + D_{w0} + D_{b0} + \mathcal{R}_0, \tag{2}$$

where P_0 is the tidal energy input, $\mathbf{F}_0$ is the horizontal barotropic flux vector, C_L is the conversion of the barotropic energy to the resolved baroclinic modes, D_{w0} is the barotropic energy loss to the wave drag, i.e., the unresolved high-mode waves, D_{b0} is the barotropic energy loss to the quadratic bottom drag, $\mathcal{R}_0$ is a residual term accounting for numerical and viscous dissipation, small nonlinear terms, and discretization errors, and subscripts "0" and "L" refer to the barotropic and the resolved baroclinic "Low" modes, respectively. The depth-integrated and time-mean baroclinic energy balance reads

$$C_L = \nabla \cdot \mathbf{F}_L + D_L, \tag{3}$$

where

$$D_L = D_{wL} + D_{bL} + \mathcal{R}_L, \tag{4}$$

$\mathbf{F}_L$ is the depth-integrated baroclinic flux vector, D_L is the low-mode dissipation, D_{wL} is baroclinic dissipation due to linear wave drag, D_{bL} is the dissipation due to bottom drag, and $\mathcal{R}_L$ is a residual term accounting for unresolved dissipation due to viscosity, small nonlinear terms, and discretization errors.

In this paper we evaluate some of the terms in Eqs. (2) and (3) for H12 and H25. We perform a least-squares harmonic analysis over a two-week-long time series to extract the M_2 harmonic constants for the 3D HYCOM fields and compute the energy terms in layer space as detailed in Buijsman et al. (2016). We limit our time series to two weeks to mitigate data storage issues: the original and interpolated time series of H12 and H25 amount to more than 100 Tera Bytes (TB) of storage. We assume that during this period the internal tides are stationary in most places, i.e., their phases and amplitudes are minimally affected by the time varying background flow (see Appendix).

2.2.2. Modal energetics

We decompose the baroclinic fields into vertical modes and compute modal energetics following Gerkema and Zimmerman (2008), Kelly et al. (2012), and Buijsman et al. (2014) to better understand the interplay between model horizontal resolution and wave drag. In a first step, we interpolate the baroclinic velocities, u and v, and the potential density referenced to 2000 decibar, ρ_2, on the hybrid coordinate grid to a z-grid with $\Delta z = 25$ m for every time step. We average the density over two weeks and compute the buoyancy frequency $N(z)$. For each horizontal grid cell, we solve the hydrostatic Stürm–Liouville equation

$$\frac{\partial^2 \mathcal{W}_n(z)}{\partial z^2} + \frac{N^2}{c_n^2}\mathcal{W}_n(z) = 0, \tag{5}$$

where $\mathcal{W}_n(z)$ is the eigenfunction of the vertical velocity of mode n, c_n is the eigenspeed, and z is the vertical coordinate. The eigenspeed is computed as

$$c_n = \frac{\sqrt{\omega^2 - f^2}}{k_n}, \tag{6}$$

where f and ω are the Coriolis and M_2 frequencies and k_n is the horizontal wave number. Note that the phase speed is $c_{pn} = \omega/k_n$ and the group speed is $c_{gn} = c_n^2 k_n/\omega$. We then compute the horizontal velocity eigenfunction

$$\mathcal{U}_n(z) = \frac{\partial \mathcal{W}_n(z)}{\partial z} \tag{7}$$

and normalize it by $\sqrt{\frac{1}{H}\int_{-H}^{0} \mathcal{U}_n^2(z)\mathrm{d}z}$, where H is the seafloor depth.

In a next step, the M_2 complex harmonic constants are extracted with a least-squares harmonic fit of the interpolated u, v, and ρ_2 time series. The perturbation pressure is computed by depth-integrating the complex harmonic constants of ρ_2 and by removing the depth-mean pressure. Then, the horizontal velocity eigenfunctions are projected onto the vertical profiles of the horizontal velocity and pressure harmonic constants to yield the complex modal amplitudes in each horizontal grid cell, e.g.,

$$\hat{u}_n = \frac{1}{H}\int_{-H}^{0} \mathcal{U}_n(z)\tilde{u}(z)\mathrm{d}z, \tag{8}$$

where $\tilde{u}$ is the complex harmonic constant of u. Each fitted mode is removed from the profiles of the complex harmonic constants before fitting the next mode to avoid overfitting.

After obtaining the eigenspeeds and complex modal amplitudes, we compute the terms in the depth-integrated and time-averaged modal energy equation (Kelly et al., 2012)

$$\underbrace{\sum_{m=0}^{5} C_{mn}}_{\text{Conversion}} = \frac{\rho_c H}{4}\left[\underbrace{|\hat{\mathbf{u}}_n|^2}_{KE} + \underbrace{\left(1-\frac{f^2}{\omega^2}\right)\frac{|\hat{p}_n|^2}{(\rho_c c_n)^2}}_{APE}\right]_t + \underbrace{\frac{1}{2}\nabla\cdot\left(H\hat{\mathbf{u}}_n^*\hat{p}_n\right)}_{\text{Flux Div.}} + \underbrace{D_n}_{\text{Dissipation}}, \quad (9)$$

where ρ_c is the space and time-invariant density, t is time, $|\hat{\mathbf{u}}_n|$ and $\hat{p}_n$ are the complex modal amplitudes of the velocity vector and perturbation pressure, * is the complex conjugate, and n and m are mode numbers. The first term on the L.H.S. of Eq. (9) is the intermodal-energy conversion and the first term on the R.H.S. is the time-mean of the rate of change of kinetic (KE) and available potential energy (APE), the second term is the energy flux divergence, and the third term is the dissipation, a residual term. The factor $\frac{1}{2}$ arises from time averaging over a tidal cycle. Note that in this case the rate of change term is close to zero, and can be ignored. We compute these terms for the first five modes because up to five modes are resolved in the H25 simulation (see next section). The barotropic to baroclinic conversion to the first five modes is $\sum_{n=1}^{5} C_{0n}$ and should be comparable to C_L of Eq. (2).

The intermodal-energy conversion term for $n > 0$ and $m > 0$ is computed as Kelly et al. (2012)

$$C_{mn} = \int_{-H}^{0} (\mathbf{u}_m^* \cdot \nabla p_n - \mathbf{u}_n^* \cdot \nabla p_m)\mathrm{d}z, \quad (10)$$

where $\mathbf{u}_n(z) = \hat{\mathbf{u}}_n \mathcal{U}_n(z)$ and $p_m(z) = \hat{p}_m \mathcal{U}_m(z)$. This mode-scattering term is non-zero when horizontal gradients in topography and stratification are present. However, C_{mn} mostly correlates with topographic gradients in our simulations. This term does not represent nonlinear mode-mode interactions, which result from the advective term in the momentum equation, ignored in this analysis. We compute $\sum_{m=1}^{5} C_{mn}$, which is the energy transfer between each mode n and the other four modes. The uncertainty for this term may be larger than for C_{0n}. The horizontal gradients in Eq. (10) are computed using central finite differences. The values of the vertical profile of $\mathbf{u}_m^*(z) \cdot \nabla p_n(z) - \mathbf{u}_n^*(z) \cdot \nabla p_m(z)$ are set to zero downslope of the shallowest seafloor depths to avoid erroneously large values. To show that this term is relevant, we compute for each mode of H25 the spatial correlation r_a between $\frac{1}{2}\nabla \cdot \left(H\hat{\mathbf{u}}_n^*\hat{p}_n\right)$ and C_{0n} and the correlation r_b between $\frac{1}{2}\nabla \cdot \left(H\hat{\mathbf{u}}_n^*\hat{p}_n\right)$ and $C_{0n} + \sum_{m=1}^{5} C_{mn}$. The inclusion of $\sum_{m=1}^{5} C_{mn}$ increases the correlation from $r_a = 0.73, 0.44, 0.29, 0.15, 0.05$ to $r_b = 0.77, 0.65, 0.54, 0.34, 0.17$ for modes 1–5 and it lowers the standard deviation of the residual dissipation D_n by maximally 13% ($\frac{-8.7\times10^{-4}\ \mathrm{W\ m^{-2}}}{68.8\times10^{-4}\ \mathrm{W\ m^{-2}}}$) for mode 2. This demonstrates that the mode-scattering term is relevant, in particular in the H25 simulation.

2.3. Resolved modes

The horizontal and vertical resolutions of the HYCOM simulations determine the number of modes that can be resolved. For the simulations considered, we find that the horizontal resolution is the limiting factor over most of the ocean area and not the vertical resolution of 41 layers. Hence, in the following we discuss the effect on the horizontal wavelength.

The stratification in both the H12 and H25 simulations is similar, yielding the same low-mode wavelengths, as computed with Eq. (6). In Fig. 1, we plot the mode-1 and 2 wavelengths of H25 as an example. Latitude, seafloor depth, and stratification affect the spatial variability in wavelengths. The wavelength of the first baroclinic M_2 mode varies from ~80 km in the eastern equatorial ocean basins to ~200 km at higher latitudes (Fig. 1a). The mode-2 wavelength is about half as long (Fig. 1b). Although not shown, the mode-1 and 2 wavelengths

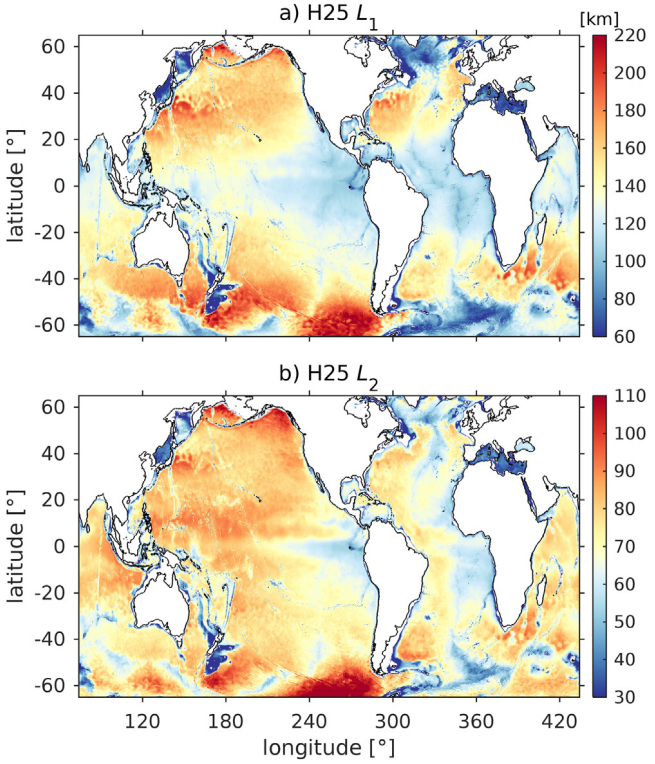

Fig. 1. The M_2 wavelength for (a) mode 1, 60 to 220 km shown, and (b) mode 2, 30 to 110 km shown, for the H25 simulation. The wavelengths are computed by solving the Stürm–Liouville equation (5).

agree with the wavelengths inferred from climatology and altimetry wave-number spectra by Ray and Zaron (2016).

We compute the number of grid cells that can fit inside the wavelengths of the first five modes: $L_n/\Delta x$, where L_n is the modal wavelength and Δx is the maximum grid spacing of each grid cell. Fig. 2 shows global maps of $L_n/\Delta x$ for the first five modes for H12 and H25. If we assume that the minimum number of grid cells needed to resolve a wave mode is five, then the first two and the first five modes are resolved in most of the global ocean in the H12 and H25 simulations, respectively. In H12, modes 3–5 are not well resolved in the equatorial and mid-latitude regions (white areas in Fig. 2). To better quantify the effect of seafloor depth on the resolved modes, we area-average $L_n/\Delta x$ for seafloor-depth bins with a width of 500 m, e.g., 250–750 m, 750–1250 m, 1250–1750 m, ... 5750–6250 m, and for latitudes equatorward of |50°| (Fig. 3). For seafloor depths deeper than 1250 m, we find that the first two and the first five modes are resolved in the H12 and H25 simulations, respectively. In the shallowest depth bin of 250–750 m, only mode 1 and the first three modes are resolved in H12 and H25, respectively. Hence, we solve for the first five modes in H12 and H25. As the waves are not well resolved in shallow water due to the horizontal model resolution and the vertical spacing of the z-grid, we do not compute modal energetics shallower than seafloor depths of 250 m.

HYCOM's horizontal grid is a C-grid (Arakawa and Lamb, 1977). A C-grid is prone to gridscale noise that is due to spatial averaging of Coriolis momentum terms and that is apparent when the grid resolution is coarse with respect to the baroclinic deformation radius (L_ρ) (Adcroft et al., 1999). According to Adcroft et al. (1999), the C-grid may cause noise when the wave resolution $r_w = 2\frac{L_\rho}{\Delta x} < 1$. We compute r_w for modes 1–5 and find that $r_w > 1$ for the resolved modes in H12 and H25, i.e., it is unlikely that these modes feed energy into short-scale perturbations that allow standing gridscale noise to persist. Such noise has not been observed in the simulations.

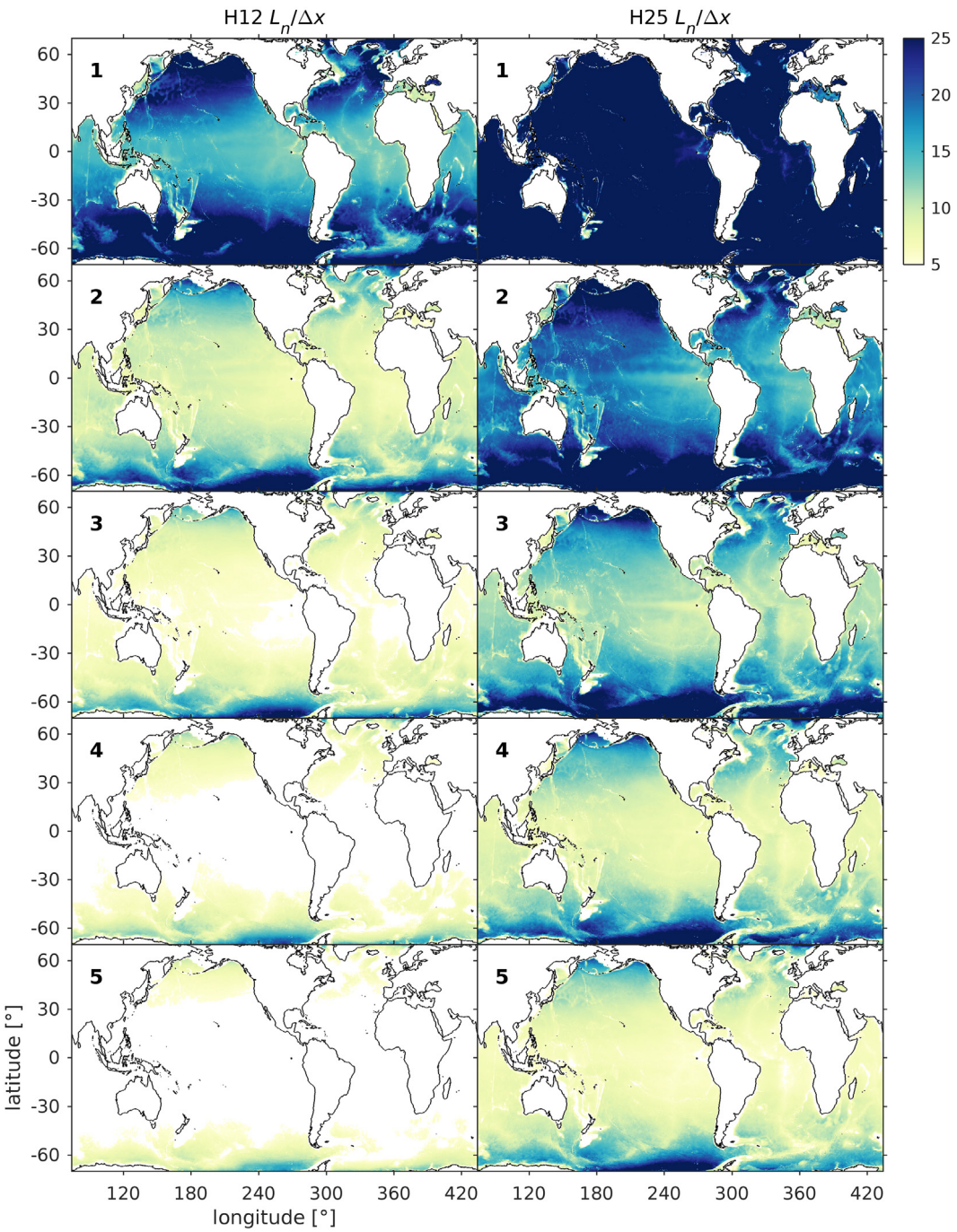

Fig. 2. The number of grid cells per wavelength $L_n/\Delta x$, where L_n is the wavelength of mode n and Δx is the maximum grid spacing of each grid cell, for the 8 km (left column) and 4 km (right column) HYCOM simulations for modes 1 to 5, as marked by the bold number in each subplot. Ocean areas where $L_n/\Delta x \leq 5$ are shaded white.

2.4. Validation data and statistical analysis

We validate our HYCOM simulations with observations and analytical model results. For some model-data comparisons, we compute the following statistics (Ansong et al., 2017): the correlation coefficient r, the ratio γ between the simulated and observed variables, and the regression coefficient A (i.e., the slope), which is obtained with a linear least-squares regression: $var_{\text{HYCOM}} = A \cdot var_{\text{observation}}$, where var is a variable. The results of the statistical analysis are in Table 1. In the following, we discuss the various validation data sets.

We compare HYCOM M_2 internal-tide sea-surface height variance computed for a two-week and one-year long time series with that extracted from 17 years of altimetry time series, which were also used by Shriver et al. (2012). We apply a least-squares harmonic fit to the altimetry and HYCOM data to extract the harmonic constants. We interpolate the harmonic constants of HYCOM to the same locations as the altimetry data for seafloor depths deeper than 1500 m. The internal tide harmonic constants are recovered from the HYCOM and altimeter data sets via along-track band-pass filtering to permit wavelengths in the 50–400 km range. At the mid-latitudes, the internal-tide length scales and periods are similar to those of the mesoscales. Hence, the non-tidal motions may be aliased into the internal-tide signals extracted from satellite altimetry (Ray and Byrne, 2010; Shriver et al., 2012). To reduce these effects, data that coincide with eddy kinetic energy $EKE > 200$ cm^2 s^{-2} are excluded from the statistical analysis. Although EKE is large near the equator, the Rossby radii are much larger than

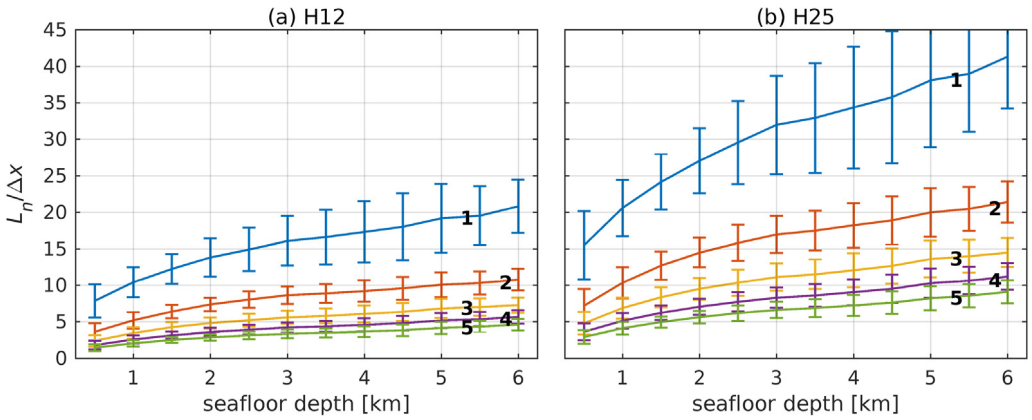

Fig. 3. The number of grid cells per wavelength $L_n/\Delta x$ for modes $n = 1-5$ (bold numbers) as a function of seafloor depth for (a) H12 and (b) H25. $L_n/\Delta x$ is area-averaged for seafloor-depth bins of 500 m ranging from 250 m to 6250 m and for latitudes equatorward of |50°|. The length of the error bars is twice the standard deviation over all $L_n/\Delta x$ in each depth bin.

Table 1
Regression coefficient A, ratio γ, and correlation coefficient r between the model and observations for global SSH variance $\sigma^2 = \frac{1}{2}|\tilde{\eta}|^2$, and global mode 1 and 2 energy fluxes. Subscripts $_{2W}$ and $_{1Y}$ refer to the two-week and one-year HYCOM time series, respectively. The statistics are computed for the absolute value and absolute magnitudes of the x and y vector components of the energy fluxes. Uncorrected/corrected indicates if the HYCOM variable is adjusted for the time series duration (see Appendix).

variable	simulation	uncorrected			corrected		
		A	γ	r	A	γ	r
σ^2_{2W}	H12	0.99	1.71	0.52	0.60	0.80	0.63
σ^2_{1Y}	H12	0.90	1.15	0.68	0.80	0.96	0.69
σ^2_{2W}	H25	1.24	2.10	0.54	0.75	1.02	0.65
σ^2_{1Y}	H25	1.08	1.28	0.77	0.97	1.09	0.78
$\lvert\mathbf{F}_1\rvert$	H25	1.82	2.85	0.54	1.29	1.61	0.60
$\lvert F_{x1}\rvert$	H25	2.35	3.88	0.49	1.68	2.17	0.55
$\lvert F_{y1}\rvert$	H25	1.38	2.27	0.53	0.98	1.29	0.58
$\lvert\mathbf{F}_2\rvert$	H25	2.20	5.04	0.35	1.56	2.79	0.41
$\lvert F_{x2}\rvert$	H25	4.41	11.54	0.25	3.12	6.34	0.30
$\lvert F_{y2}\rvert$	H25	1.56	3.44	0.38	1.11	1.93	0.44

the internal-tide wavelengths. Hence, we do not omit data for latitudes (ϕ) equatorward of |20°|. This EKE data set is based on surface drifter velocities from the Global Drifter Program and is adapted from Whalen et al. (2012).

We compare the area-integrated loss of surface-tide energy in HYCOM to the barotropic dissipation inferred from TPXO8-atlas. These dissipation rates are computed as the residual of the sum of the tidal energy input and barotropic flux divergence (Green and Nycander, 2013). The dissipation rates used here have also been used in Buijsman et al. (2015).

The globally-integrated modal conversion rates of HYCOM are compared with the rates from analytical models by Falahat et al. (2014) and Vic et al. (2019). In these analytical models, the conversion rates are computed by multiplying a linear wave drag parameterization, based on theory by Bell (1975), with barotropic tidal velocities from the TPXO tide model. As in Vic et al. (2019), we do this comparison for seafloor depths > 700 m because the linear analytical models do not well predict conversion rates at supercritical slopes.

We compare the mode-1 and 2 fluxes of H25 to the energy fluxes that are extracted from altimetry data sets with a plane-wave fit method by Zhao et al. (2016) and Zhao (2018). The plane-wave fit method yields fluxes for three directions. We use their vector sum for the comparison. The HYCOM fluxes are averaged to the Cartesian 0.2° grid of the altimetry data to facilitate the statistical analysis. Data that coincide with $EKE > 200$ cm^2 s^{-2} (except for $|\phi| < 20°$) are excluded from this analysis.

3. Results

3.1. Undecomposed fields

3.1.1. M_2 internal-tide sea-surface-height variance

Before considering the tidal energetics, we compare the stationary M_2 internal-tide sea-surface-height variance of H12 and H25 to altimetry. The variance is computed as $\sigma^2 = \frac{1}{2}|\tilde{\eta}|^2$, where $\tilde{\eta}$ is the complex harmonic constant computed over the two-week and one-year long time series. The sea-surface-height variance is mostly dominated by the low vertical modes. The internal-tide SSH variance of the two-week long uncorrected H12 and H25 time series ($\sigma^2{}_{2W}$) in Fig. 4a and b is about twice as large as the variance of the altimetry in Fig. 4i and Table 1. The mean variance in H12 and H25 in the hotspot regions is respectively 71% ($\frac{0.22\ \text{cm}^2}{0.30\ \text{cm}^2}$) and 108% ($\frac{0.33\ \text{cm}^2}{0.30\ \text{cm}^2}$) larger than the altimetry variance. Averaged over the global ocean, the variance in H12 and H25 is 71% ($\frac{0.08\ \text{cm}^2}{0.11\ \text{cm}^2}$) and 110% ($\frac{0.12\ \text{cm}^2}{0.11\ \text{cm}^2}$) larger, respectively. The correlation between the simulated variance and the altimetry is modest, albeit that it is slightly better for H25 ($r = 0.54$) than for H12 ($r = 0.52$; Table 1). When we compare the H12 to the H25 simulations, we find that the H25 simulation is about 21% ($\frac{0.11\ \text{cm}^2}{0.52\ \text{cm}^2}$) more energetic than H12 in the hotspot regions, whereas in a globally-integrated sense, H25 is 23% ($\frac{0.04\ \text{cm}^2}{0.19\ \text{cm}^2}$) more energetic than H12. This difference is because the Atlantic Ocean, which does not have hotspot boxes, is more energetic in H25 than in H12.

It is to be expected that the stationary variance for the two-week long HYCOM time series is larger than the variance extracted from the 17-year long altimetry time series because the stationary variance decreases with the time-series duration (Appendix). To illustrate this point, we also compute the M_2 variance for the one-year long HYCOM time series ($\sigma^2{}_{1Y}$; Fig. 4c and d). The largest differences between $\sigma^2{}_{2W}$ and $\sigma^2{}_{1Y}$ occur in areas with the strongest time variability in subtidal background flows, such as in the equatorial Pacific (Buijsman et al., 2017). Although $\sigma^2{}_{1Y}$ is smaller than $\sigma^2{}_{2W}$, the globally-averaged $\sigma^2{}_{1Y}$ is still larger than the altimetry variance by 15% ($\frac{0.02\ \text{cm}^2}{0.11\ \text{cm}^2}$) and 28% ($\frac{0.03\ \text{cm}^2}{0.11\ \text{cm}^2}$) for H12 and H25, respectively. This difference is larger in the hotspot regions: 36% ($\frac{0.11\ \text{cm}^2}{0.30\ \text{cm}^2}$) and 43% ($\frac{0.13\ \text{cm}^2}{0.30\ \text{cm}^2}$) for H12 and H25, respectively. The correlation between the year-long HYCOM and altimetry variance is better than for the two-week time series: $r = 0.68$ for H12 and $r = 0.77$ for H25 (Table 1).

To ensure a more apples to apples comparison, we correct the HYCOM variance for the two-week and one-year long time series with a spatially varying correction coefficient, which is close to unity in the nearfield and small in the farfield. This correction coefficient is derived in the Appendix using an older six-year long 8-km HYCOM simulation. The corrected M_2 SSH variance for the two-week long time

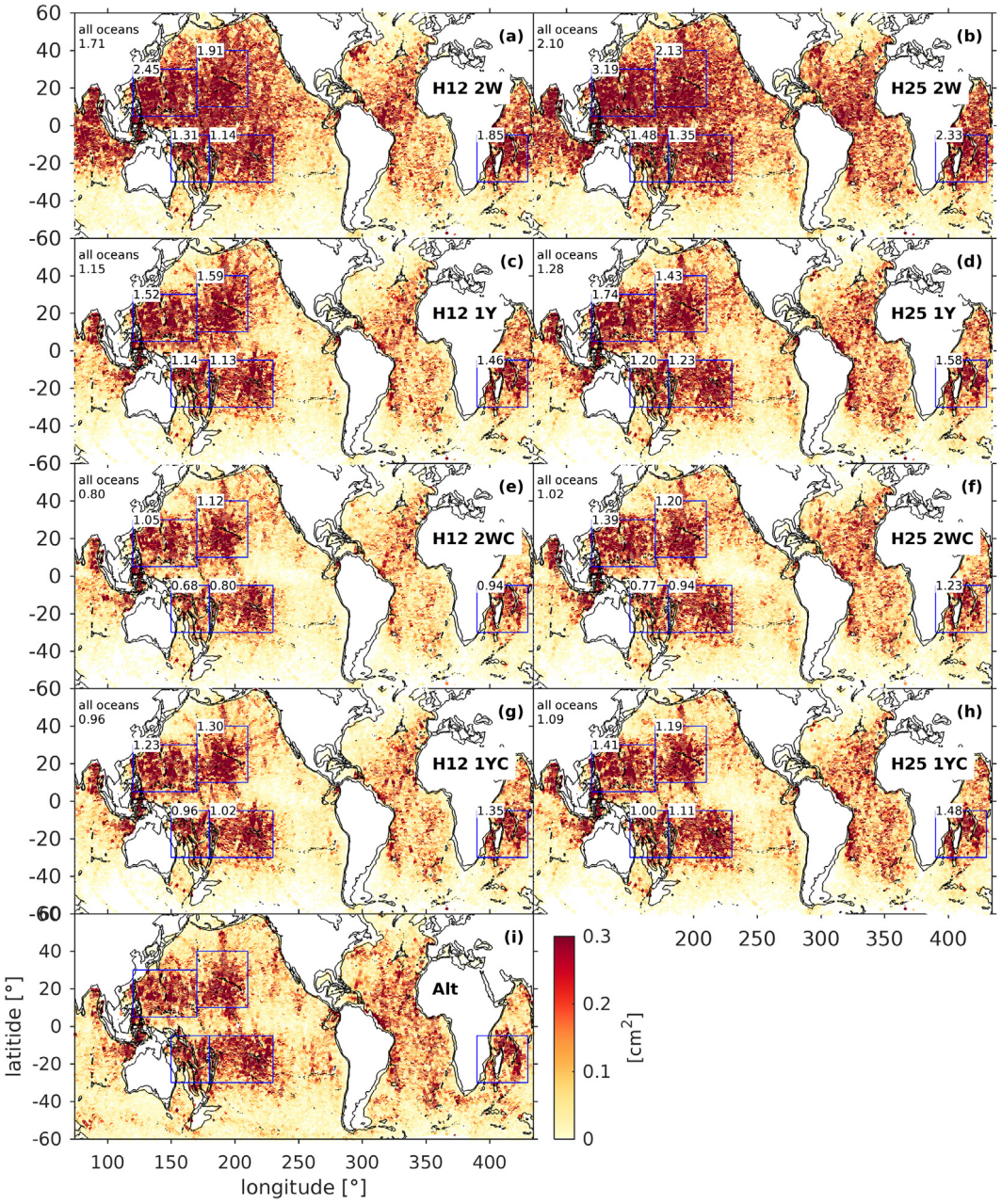

Fig. 4. M_2 internal-tide SSH variance for (a–h) the H12 and H25 simulations and (i) the altimetry. The uncorrected HYCOM variance is in (a–d) while the corrected variance ('C') is in (e–h). The variance based on the two-week ('2W') long time series is shown in (a, b) and (e, f). The variance based on the one-year ('1Y') long time series is shown in (c, d) and (g, h). The 0 and 2000 m seafloor depths are plotted as the black contours. The numbers represent γ, the simulated variance normalized by the observed variance. γ is computed for the internal-tide generation hotspots (boxes) and the global ocean (top left of each subplot) excluding areas where $EKE > 200$ m^2 s^{-2} coincides with $|\phi| > 20°$.

series ($\sigma^2{}_{2WC}$) and the one-year long time series ($\sigma^2{}_{1YC}$) are shown in Fig. 4e and g for H12 and in Fig. 4f and h for H25. Although the correction factor reduces the variance more for the two-week than for the one-year long time series, the corrected variance of H12 and H25 for both durations is approximately similar to the altimetry variance. In accordance, the relative increase in the correlation coefficient due to the correction is larger for the two-week time series (Table 1). While the corrected variance for H12 is generally underpredicted, the corrected variance for H25 is overpredicted for both durations. The agreement for the one-year long H25 time series is the best, with γ, r, and A being the closest to unity (Table 1). After correction, the mean variance of the two-week long H25 time series is 11% ($\frac{0.03\ \text{cm}^2}{0.30\ \text{cm}^2}$) larger than the altimetry variance in the hotspot regions, while it is only 2% ($\frac{0.002\ \text{cm}^2}{0.110\ \text{cm}^2}$) larger when averaged over the global ocean. In contrast, the mean variance of the one-year long time series is 23% larger ($\frac{0.07\ \text{cm}^2}{0.30\ \text{cm}^2}$) in the hotspot regions and 9% ($\frac{0.01\ \text{cm}^2}{0.11\ \text{cm}^2}$) larger over the global ocean.

3.1.2. *Barotropic and baroclinic M_2 energetics*

For H12 and H25, we compute the time-mean, depth-integrated, and global area-integrated energy input $\{P_0\}$, the barotropic conversion to the resolved internal tides $\{C_L\}$, the barotropic loss to the wave drag $\{D_{w0}\}$, the barotropic energy loss to the resolved and unresolved wave modes $\{C_L + D_{w0}\}$, and the energy loss of the resolved internal tides to the wave drag $\{D_{wL}\}$, where $\{.\}$ indicates an area integration (Fig. 5). The M_2 energy input and the barotropic energy loss to the internal tides are also computed for TPXO8-atlas data (Green and Nycander, 2013) and compared with the HYCOM simulations. $\{P_0\}$ is computed for all seafloor depths, while the other terms are computed for seafloor depths

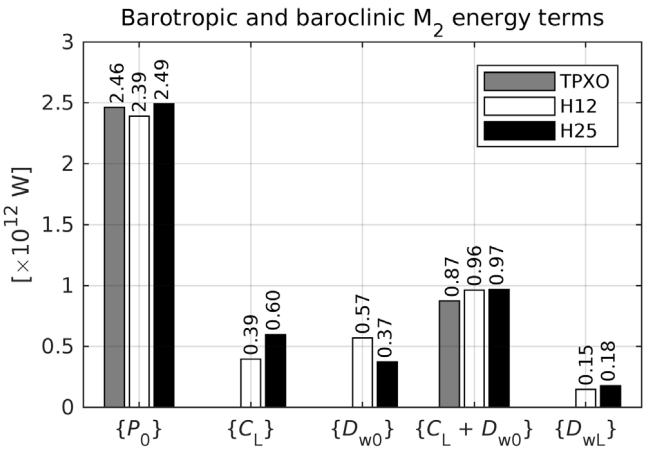

Fig. 5. Globally- and depth-integrated tidal-mean M_2 barotropic and baroclinic energy terms from Eqs. (2)–(4) for TPXO8-atlas and the H12 and H25 simulations ({.} indicates area-integrated quantities). $\{P_0\}$ is computed for all seafloor depths, while the other terms are computed for seafloor depths deeper than 250 m.

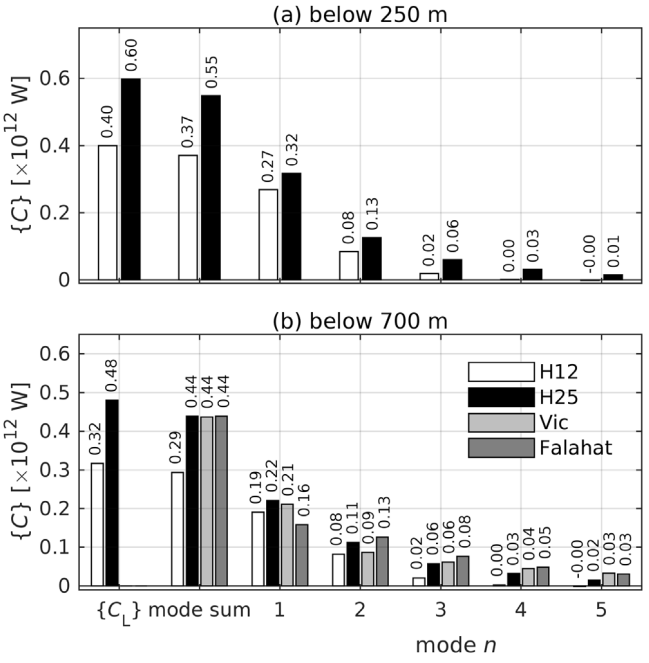

Fig. 6. Time-mean and globally-integrated energy conversion rates from the barotropic tide to the first five baroclinic modes ($\{C_{0n}\}$) for the H12 and H25 simulations for seafloor depths (a) >250 m and (b) >700 m. For comparison, the conversion computed without doing the modal decomposition ($\{C_L\}$) is also plotted. In (b) the HYCOM rates are compared with the rates from the analytical conversion models by Vic et al. (2019) and Falahat et al. (2014).

deeper than 250 m. The TPXO8-atlas dissipation includes both surface tide energy loss to the internal tides and bottom drag. The former occurs in deep water, while the latter occurs primarily in coastal shelf seas shallower than 250 m. The energy input for both HYCOM solutions compares well with that of TPXO. In H25, the resolved barotropic to baroclinic energy conversion $\{C_L\}$ is about 0.21 TW larger than in H12. This increase in the conversion in H25 is offset by a near-equal reduction of 0.20 TW in the energy conversion to the unresolved modes $\{D_{w0}\}$ in H25. As a consequence, $\{C_L + D_{w0}\}$ is about the same for both H12 and H25 simulations. This result is consistent with both simulations having the same tidal accuracy and energy input. $\{C_L + D_{w0}\}$ is about 11% ($\frac{0.09\ \text{TW}}{0.87\ \text{TW}}$) larger than the deep-water barotropic dissipation of TPXO, which is a fairly good agreement. The weaker drag scale in H25 yields a smaller D_{w0} as compared to H12. At the same

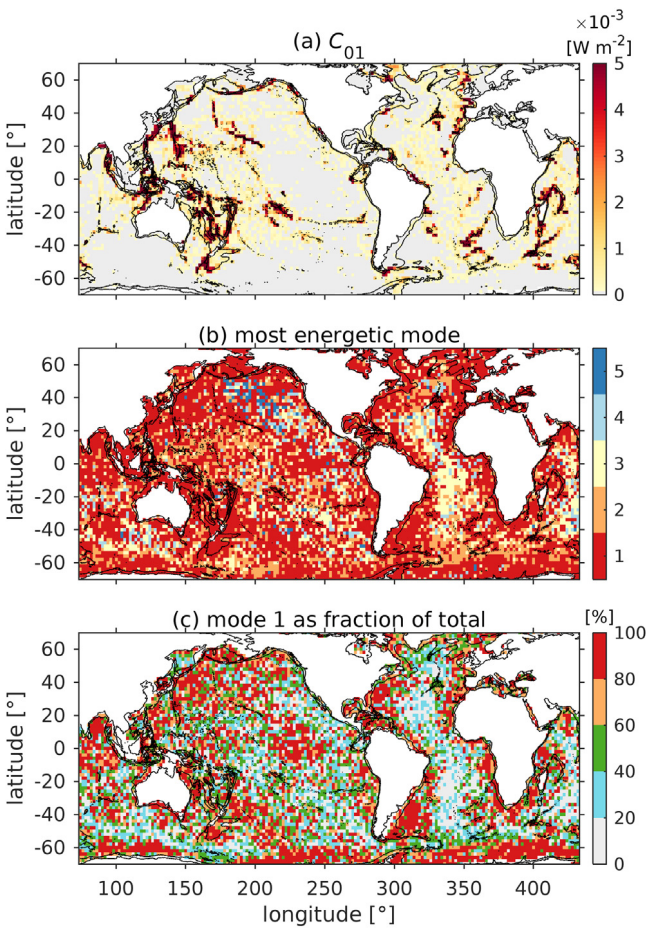

Fig. 7. (a) The barotropic to baroclinic energy conversion to mode 1 (C_{01}). (b) The mode number n with the largest absolute conversion $|C_{0n}|$. (c) The mode-1 conversion as fraction of the sum over the first five modes. The absolute fraction is plotted. All values are from H25 and averaged to 2° × 2° bins.

time, H25 resolves more higher modes, increasing C_L. The increase of C_L in H25 relative to H12 is the largest over the deeper mid-ocean ridges (not shown), which are more efficient higher-mode generators. In contrast, the differences in C_L at the tall mid-ocean ridges, such as Hawaii, are smaller because the conversion at these ridges is mostly due to low modes, which are both resolved in H12 and H25. Although the drag scale is smaller for H25, the internal tide energy loss to the wave drag ($\{D_{wL}\}$) is about the same in H12 and H25 because H25 features more internal tide energy. In the next section, we discuss the modal decomposition of this energy.

3.2. Modal M_2 energetics

3.2.1. Internal tide generation

As the surface tide oscillates over underwater topography, surface tide energy is transferred to baroclinic modes. The global integral of the time-mean barotropic to baroclinic conversion to the full spectrum of the resolved internal tides ($\{C_L\}$ of Eq. (2)) and to the first five modes ($\{C_{0n}\}$ of Eq. (9)) is presented in Fig. 6. The rates computed for seafloor depths > 250 m are shown in Fig. 6a. In the open ocean, most of the surface tide energy is converted into mode 1 in the H12 and H25 simulations. However, the higher horizontal resolution of H25 resolves more higher vertical modes than H12. $\{C_{01}\}$ of H25 is 19% ($\frac{0.05\ \text{TW}}{0.27\ \text{TW}}$) larger than that of H12. The increase in the mode-1 conversion may be attributed to a better-resolved bathymetry in H25. The mode-2 conversion is 63% ($\frac{0.05\ \text{TW}}{0.08\ \text{TW}}$) larger in H25, and this difference becomes much larger for higher modes. The sum of the conversion over all

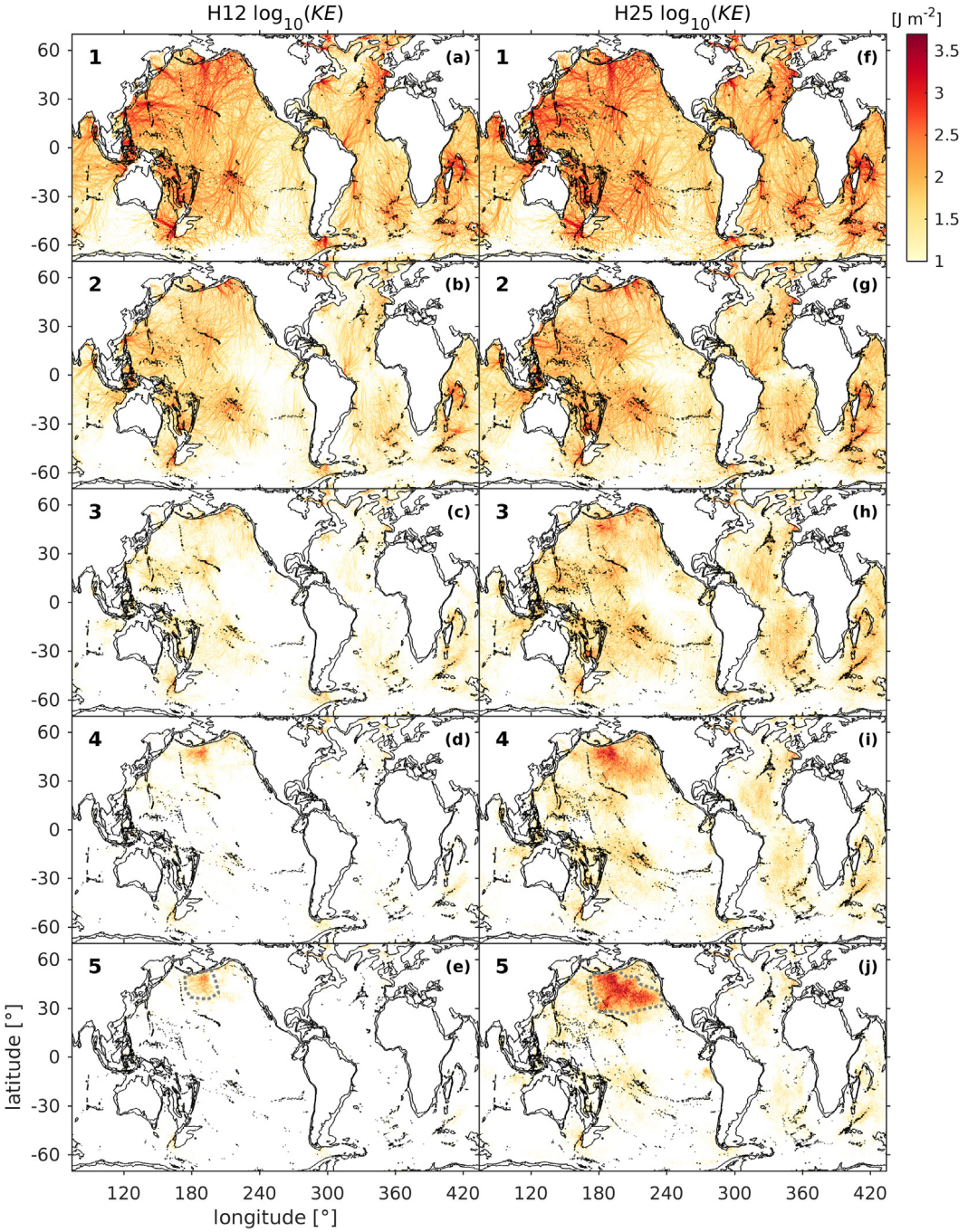

Fig. 8. Depth-integrated modal baroclinic kinetic energy for the 8 km (a–e) and 4 km (f–j) HYCOM simulations for modes 1 to 5, as marked by the bold number in each subplot. The gray dotted polygons in (e) and (j) mark the boundaries of the areas with thermobaric instabilities that are excluded from some of the analyses discussed in the text.

modes is about 8% smaller than the undecomposed conversion $\{C_L\}$ for both H12 ($\frac{-0.03\ \text{TW}}{0.40\ \text{TW}}$) and H25 ($\frac{-0.05\ \text{TW}}{0.60\ \text{TW}}$). The difference may be due to missed higher modes, imperfect modal fits, and interpolation errors.

We also compare the HYCOM conversion rates to the rates computed with the analytical models of Vic et al. (2019) and Falahat et al. (2014) for seafloor depths > 700 m in Fig. 6b. Compared to the analytical conversion rates, H25 performs quite well for modes 1 to 4, while only modes 1 and 2 of H12 compare well with the analytical rates. The mode-5 conversion of H25 is about 30% ($\frac{-0.01\ \text{TW}}{0.03\ \text{TW}}$) smaller than the analytical rates. We note that for H12 and H25 about 30% ($\frac{0.08\ \text{TW}}{0.27\ \text{TW}}$ and $\frac{0.10\ \text{TW}}{0.32\ \text{TW}}$) of the mode-1 conversion occurs in the seafloor-depth range of 250–700 m. This implies that the choice of the minimum cutoff depth can impact global energy budget calculations.

To visualize the spatial distribution of the modal conversion rates in H25, we average the rates to 2°×2° bins (Fig. 7). This procedure reduces the visually distracting presence of negative conversion rates, which occur when the perturbation pressure is out of phase with the local barotropic velocities, i.e., energy is transferred from the internal to the surface tide (Simmons et al., 2004; Buijsman et al., 2010; Kelly and Nash, 2010). The mode-1 conversion rates in Fig. 7a are largest at tall ocean ridges, e.g., in the western Pacific and Indian Ocean, and along some continental shelves, e.g., the Bay of Biscay and the Amazon shelf. Although the appearance of the most energetic mode in Fig. 7b and the mode-1 conversion as fraction of the first five modes in Fig. 7c is noisy, large-scale patterns are visible. These patterns are in agreement with results by de Lavergne et al. (2019) and Vic et al. (2019). In

most of the ocean, the mode 1 conversion dominates in H25, while modes 2–4 are relatively more important at the flat and wide mid-ocean spreading ridges, such as the Mid-Atlantic Ridge, the Southwest and Central Indian Ridges, and the East Pacific Rise (Fig. 7b and c). At these deep ridges, mode 1 comprises less than 20% ($\frac{0.11\ \text{TW}}{0.55\ \text{TW}}$) of the conversion to the first five modes (Fig. 7c).

3.2.2. Internal-tide propagation

Next, we evaluate the energy density and energy fluxes to better understand the propagation of the internal-tide modes in H12 and H25. In Fig. 8, we present maps of the kinetic energy (KE) for the first five modes for H12 and H25. Maps of the available potential energy (APE) are similar and are not shown. In both H12 and H25, beams of mode-1 energy radiate away from generation hotspots, such as the Hawaiian, Polynesian, and Mariana ridges in the Pacific, Georges Bank, and the Amazon shelf in the Atlantic, and the Mascarene, Nicobar, and Andaman island ridges in the Indian Ocean (Fig. 8a and f). The lengths of some mode-1 beams are longer than 3000 km, reflecting the low decay rates of the mode-1 waves.

Beams of mode-2 energy are not as intense nor do they propagate as far, but strong signals extend hundreds of kilometers away from generation sites, such as the Amazon shelf, the Mascarene Ridge, and the Aleutians (Fig. 8b and g). While the difference in mode-1 energy density between H12 and H25 is relatively small, the mode-2 beams of H25 are more energetic than those of H12.

For baroclinic modes 3 to 5, more differences are evident in the kinetic energy maps for H12 and H25 (Fig. 8c–e and h–j). For H12, little to no high-mode energy is present in areas where $L_n/\Delta x < 5$ in Fig. 2. At higher latitudes, where the grid spacing decreases, some energy is present equatorward of the turning latitude (74.5° for the M_2 tide), for example south of Tasmania. In H25, baroclinic kinetic energy in modes 3 to 5 is found near topography in the interior ocean, especially near island chains like Hawaii, Polynesia, Indonesia, Madagascar, and along the Mid-Atlantic Ridge. In contrast to modes 1 and 2, higher-mode beams are more diffusive and harder to distinguish. This may be attributed to higher modes having more generation sites than modes 1 and 2, topographic scattering, wave–wave interactions, and refraction by the background flow, to which higher modes are more susceptible than low modes (Rainville and Pinkel, 2006).

There is a patch of elevated energy for modes 3 to 5 in the north Pacific in both simulations (Fig. 8c–e and h–j). This is likely caused by a thermobaric instability (TBI) (Hallberg, 2005) – a numerical instability in isopycnal/hybrid models that implement thermobaricity as a perturbation from reference compressibility states. The TBI effect is larger in H25 because the instability has a strong vertical shear that projects onto the higher modes. TBI mostly affects the energy density, energy fluxes, and dissipation of modes 3 to 5, whereas the conversion and topographic scattering are not much affected. We note that the TBI noise differs from gridscale noise associated with C-grids (Adcroft et al., 1999) because in the former progressive high-mode waves are generated, while in the latter standing noise patterns are generated. We do not observe these standing noise patterns in H12 and H25.

We compute global integrals of the modal KE and APE and the sum over all modes for seafloor depths > 250 m (Fig. 9). The energy density of modes 3–5 inside the polygons, marking the extent of the TBI areas in Fig. 8e and j, is excluded from the analysis. On average, $\{KE\}$ is about 15% larger than $\{APE\}$ for both H12 and H25 (ignoring modes 3–5 of H12). H25 has more total energy than H12 for all modes: 34% ($\frac{22.0\ \text{PJ}}{64.2\ \text{PJ}}$) more in mode 1, 68% ($\frac{15.4\ \text{PJ}}{22.6\ \text{PJ}}$) more energy in mode 2, and increasingly more for higher modes. Note that this 34% increase in mode-1 energy is of the same order of magnitude as the 23% increase in two-week SSH variance in H25 relative to H12 (Fig. 4). Summed over all modes, $\{KE\}$, $\{APE\}$, and their sum are about 60% larger in H25 than in H12. The globally integrated kinetic, available potential, and total energies of H25 are 84 PJ, 69 PJ, and 153 PJ, respectively, of which mode 1 comprises about 56%.

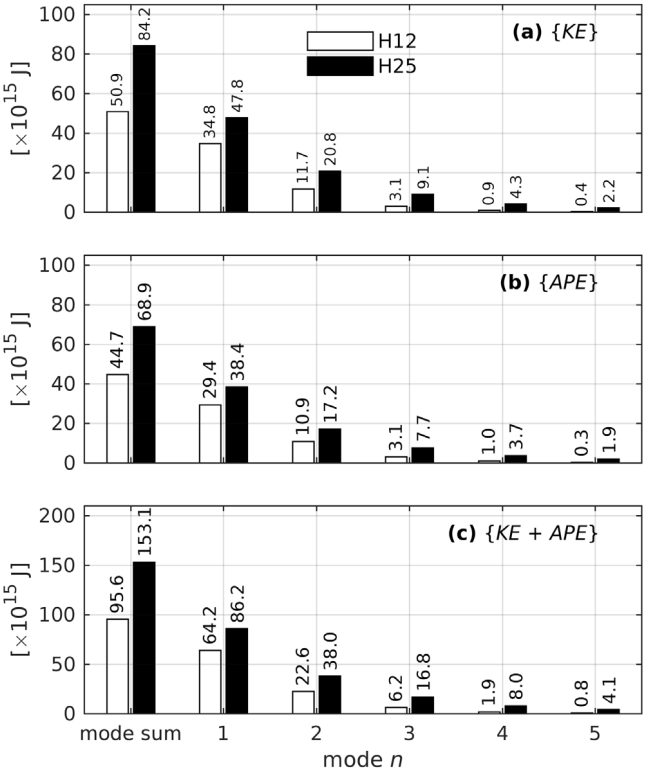

Fig. 9. Globally and depth-integrated, time-mean (a) kinetic energy and (b) available potential energy, and (c) their sum for modes 1 through 5 for the 8 km and 4 km simulations. Values are only shown for seafloor depths larger than 250 m. Modes 3–5 in the TBI areas in the North Pacific (Fig. 8e and j) are excluded from the calculations.

We compare the uncorrected and corrected M_2 mode-1 and mode-2 fluxes of H25 with the mode-1 and mode-2 fluxes extracted from altimetry in Fig. 10 and Table 1. The uncorrected mode-1 and mode-2 fluxes of H25 in Fig. 10a and d are larger than the altimetry fluxes in Fig. 10c and f. The differences are largest for the mode-2 fluxes. The application of the spatially-varying correction factor (Appendix) to the H25 fluxes improves the agreement with the altimetry (Fig. 10c and e). The correction factor is the same for both SSH variance and fluxes because both scale with u^2. The improvement is most noticeable in the equatorial Pacific. After the correction, the regression (A), ratio (γ), and correlation (r) coefficients are closer to unity for the magnitude and the x and y vector components of the energy flux (Table 1). Of all the vector components, the correlation is the largest for the absolute mode-1 flux ($|\mathbf{F}_1|$). The correlation has improved from 0.54 to 0.60 after correction. Due to the aforementioned north–south bias of the altimetry, the model correlates better with the altimetry for F_y than for F_x. The coefficients A, γ, and r for the flux comparison deviate more from unity than the coefficients computed for the SSH variance (Table 1). This is particularly true for the mode-2 fluxes. In addition to the north–south bias, other reasons for this deviation may be that the plane-wave fit yields a more diffuse beam field than the simulated wave field and that the location of some beams is incorrectly predicted by HYCOM.

3.2.3. Mode scattering

Propagating low-mode internal tides may scatter to higher modes at spatially varying underwater topography and stratification. The low-mode scattering in the H12 and H25 simulations is mostly due to topographic gradients. The scattering process is represented by C_{mn}, for $m > 0$ and $n > 0$. The global integral of $\sum_{m=1}^{5} C_{mn}$ for seafloor depths deeper than 250 m is shown in Fig. 11 for both the H12 and H25 simulations. $\sum_{m=1}^{5} C_{mn}$ is negative for mode 1 and positive for modes

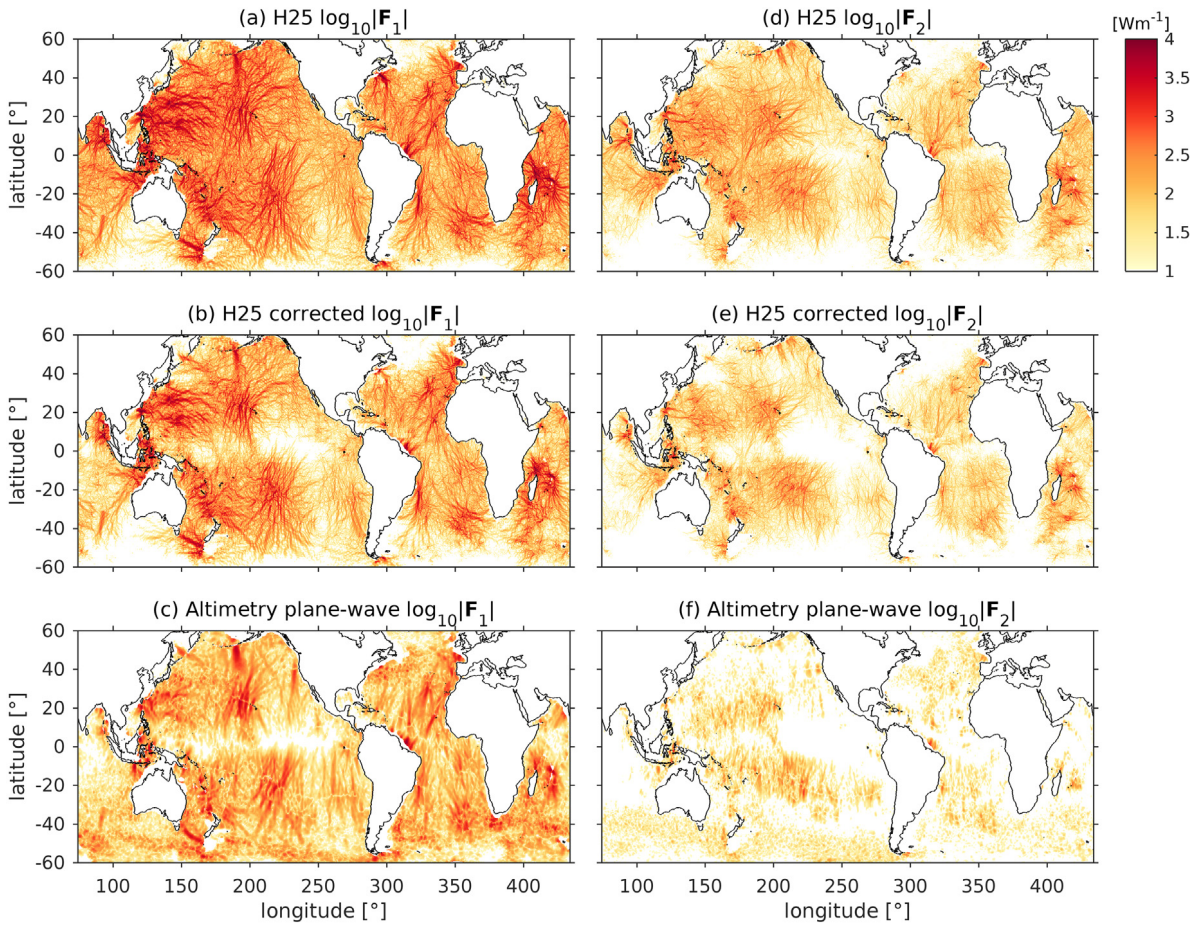

Fig. 10. Comparison between the (a and d) uncorrected and (b and e) corrected mode 1 and 2 fluxes of H25 on the one hand and (c and f) the mode 1 and 2 fluxes inferred from altimetry on the other.

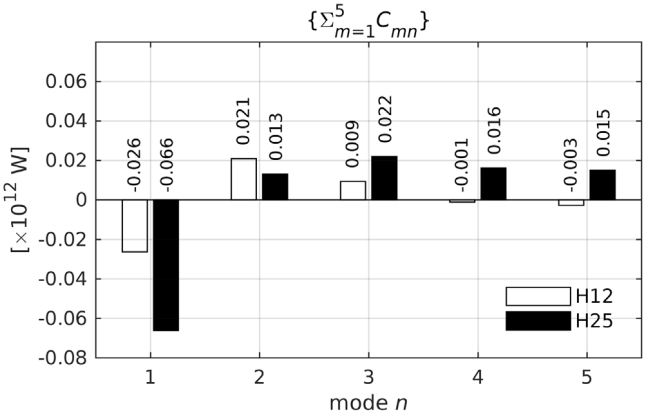

Fig. 11. Globally-integrated baroclinic mode to mode energy conversion, $\sum_{m=1}^{5} C_{mn}$, for the 8-km (H12) and 4-km (H25) HYCOM simulations. Negative values reflect an energy transfer from mode 1 to the other modes.

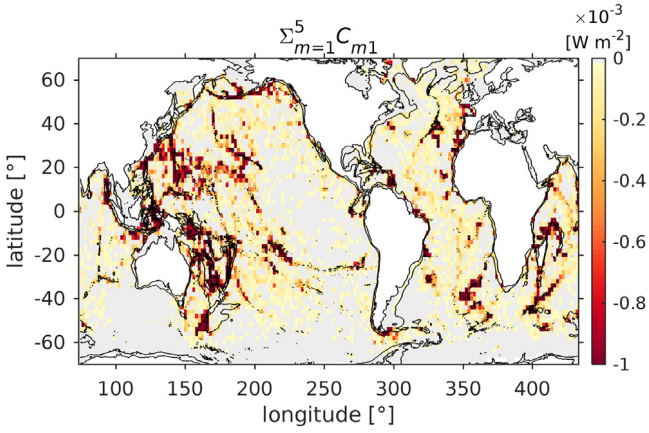

Fig. 12. The mode-1 energy conversion to modes 2–5 for H25. $\sum_{m=1}^{5} C_{m1}$ is averaged to $2° \times 2°$ bins to reduce noise. For a comparison with C_{01}, this figure's colormap is the same as in Fig. 7a, but reversed.

2–5, implying that energy is transferred from mode 1 to higher modes. The scattering out of mode 1 is about twice as strong in H25 because H25 has a better resolved bathymetry and it resolves more higher modes than H12. For H12 and H25, $\sum_{m=1}^{5} C_{m1}$ is about 10% ($\frac{0.03\ \text{TW}}{0.27\ \text{TW}}$) and 20% ($\frac{0.07\ \text{TW}}{0.32\ \text{TW}}$) of C_{01}, respectively. This fraction is of the same magnitude as the estimate by de Lavergne et al. (2019), who found that 19% of mode 1 is scattered by hills (thus excluding continental shelf topography), but lower than the estimate by Eden and Olbers (2014), who found that 53% of mode 1 is scattered at both hills and shelves.

The spatial variability of the energy scattered from mode 1, $\sum_{m=1}^{5} C_{m1}$, is highlighted in Fig. 12. As for the conversion in Fig. 7a, we average $\sum_{m=1}^{5} C_{m1}$ to $2° \times 2°$ bins to better visualize the spatial trends. Overall, $\sum_{m=1}^{5} C_{m1}$ is negative, although some randomly distributed positive values occur, which are invisible due to the choice of colormap. Similar to the energy conversion from the surface tide to mode 1 (Fig. 7a), the energy scattered out of mode-1 is also large at steep topography, such as mid-ocean ridges, hills, islands, and shelves

(Fig. 12). In contrast to the energy conversion from the surface tide to mode-1, the conversion from mode 1 to higher modes is relatively more important at the slightly wider and deeper ridges and hills, such as the Mid-Atlantic Ridge, the Line Islands Ridge south of Hawaii (Johnston et al., 2003), and the Mascarene Plateau north of Madagascar in the Indian Ocean.

3.2.4. Synthesis of the baroclinic energy balance

In this section we discuss the relevant energy terms as a function of seafloor depth. Fig. 13 shows the total energy and the terms from the modal and undecomposed baroclinic energy balances for the H12 and H25 simulations. We compare the modal energy terms of Eq. (9), summed over the first five modes (solid black, blue, and red lines in Fig. 13), with the undecomposed energy terms of Eq. (3) (same-colored dotted lines). The summed modal terms generally demonstrate the same trends as the undecomposed terms, but they are slightly smaller. This shows that the modal computations are credible, even though they are based on depth-interpolated fields. All energy terms have larger amplitudes in H25 as compared to H12, which is attributed to the larger contribution of the higher modes in H25.

The total energy in Fig. 13a and b is proportional to the binned seafloor area ($r = 0.99$; Fig. 13b) and reaches a maximum for seafloor depths of about 4500 m. The mode 1 energy of H12 is about the same as in H25 (Fig. 13a and b). The difference between the modal sums of the energy densities of H12 and H25 is largest over the deeper ridges, where more higher modes are generated (see also Fig. 7b and c).

In contrast to the depth-integrated energy, a relatively large fraction of the total conversion occurs in shallow water. About 31% ($\frac{0.10\ \text{TW}}{0.33\ \text{TW}}$) of the mode-1 conversion and 21% ($\frac{0.12\ \text{TW}}{0.56\ \text{TW}}$) of the conversion to modes 1–5 occurs for seafloor depths < 750 m. For larger seafloor depths, the conversion portrays a linear decline with depth. In both H12 and H25, the flux divergence is positive for seafloor depths shallower than 3 km, while it is negative for larger depths (Fig. 13c and d). This pattern reflects an energy flux from shallow water, where the conversion is large, to deeper water, where the energy and dissipation are large.

The large conversion for the shallow seafloor depth bin of 250–750 m coincides with relatively large dissipation rates (Fig. 13c and d). Both can be attributed to mode 1, which is the most dominant mode at tall and steep topography. In H12 and H25 about 75% ($\frac{62\ \text{GW}}{83\ \text{GW}}$) and 62% ($\frac{63\ \text{GW}}{102\ \text{GW}}$) of the mode 1 conversion is locally dissipated. Hydraulic jumps and lee waves, which can occur at tall ridges (Legg and Huijts, 2006), are not well resolved in HYCOM simulations. This may inflate the modeled dissipation rates relative to values in the actual ocean. In idealized high-resolution simulations that resolve breaking lee waves, the local dissipation fraction is about 10%–40% (Buijsman et al., 2012; Alford et al., 2015), which is lower than observed in HYCOM. In deep water the dissipation in Fig. 13c and d is attributed to the remotely-generated low modes and locally-generated higher modes. For seafloor depths of 4500 m, about 40% of the dissipation over modes 1–5 is due to mode 1 in H25. The dissipation in H25 is about 50% ($\frac{0.19\ \text{TW}}{0.40\ \text{TW}}$) larger than in H12 (red solid and dotted lines in Fig. 13c and d), which is due to the increase in (high-mode) internal tide energy in H25. The increase in the energy density in H25 has contributed to a 21% ($\frac{0.03\ \text{TW}}{0.15\ \text{TW}}$) increase in the baroclinic drag loss (D_{wL}; gray dashed line in Fig. 13c and d), despite the 40% ($\frac{-0.2}{0.5}$) reduction in drag scale in H25. The difference between D_{wL} and D_{L} (red dotted line) represents the viscous and numerical dissipation, nonlinear wave–wave interaction, and wave-scattering terms. This difference is largest in shallow water due to the relatively large conversion rates and the small baroclinic drag loss, which peaks for seafloor depths of about 3500 m.

4. Discussion

4.1. Interplay between model resolution and wave drag

The reduction in HYCOM's horizontal grid spacing from 8 to 4 km has resulted in the generation of more higher wave modes in H25 (Figs. 5 and 6). While in H12 only 2 modes are resolved, in H25 up to 5 modes are resolved. We emphasize that the horizontal and not the vertical resolution is the limiting factor in the number of modes that can be resolved in our simulations. The increase in resolved high-mode conversion in H25 is offset by a decrease in surface-tide energy loss to the wave drag (D_{w0}; Fig. 5a), which parameterizes the energy conversion to the unresolved high modes. This reduction in wave drag loss by the surface tide is due to a reduction in the drag scale by 40%, which is tuned in the H12 and H25 simulations to optimize the barotropic tidal accuracy. Since the wave drag also operates on the internal tides, one may expect that a 40% reduction in drag strength will further increase the internal tide energy in H25. Since mode 1 is the dominant mode, we will evaluate the impact of this drag scale reduction on mode 1.

In a linear system, the reduction in wave drag damping may increase the mode-1 energy by a factor $1/(1 - 0.4) = 1.67$ (a 67% increase). Compared to H12, the mode-1 conversion has increased by about 19% in H25 (Fig. 6). This implies that the energy can increase by a factor $1.67 \times 1.19 = 1.98$ (a 98% increase). However the mode-1 energy has increased by only 34% in H25 (Fig. 9). The difference between these numbers may be attributed to an increase in the scattering of mode-1 waves to higher modes at topography (Fig. 11), non-linear wave–wave interactions (Müller et al., 2015; Ansong et al., 2018), and numerical and viscous dissipation (Fig. 13) in the H25 simulation as compared to the H12 simulation. Ansong et al. (2018) find that about 0.04 TW is lost to parametric subharmonic instability (PSI) from the semidiurnal internal tide in 4-km HYCOM simulations. This is of the same order of magnitude as the energy lost from mode 1 due to topographic scattering (0.066 TW).

4.2. How realistic are the internal tides in HYCOM?

As explained in the Introduction, no other realistically-forced global ocean model has been validated as thoroughly as HYCOM (see Arbic et al., 2018 for a recent accounting of our many model-data validation efforts). In this paper, we have validated the internal tides in the H12 and H25 simulations with altimetry-derived SSH variance and energy fluxes, TPXO8-atlas surface tide dissipation rates, and conversion rates estimated from analytical models. In addition, these simulations have also been compared to mooring data in Savage et al. (2017a), Ansong et al. (2017), and Luecke et al. (2020). Overall, the H25 simulation is in better agreement with observations and analytical models than H12. Hence, we will only discuss H25 in this section. We note that H12 is an improvement over the 8-km HYCOM simulation discussed in Shriver et al. (2012) and Buijsman et al. (2016) because the surface tides in H12 are more accurate, H12 has 41 layers as opposed to 32, and the wave-drag damping is less in H12. For example, the uncorrected global-mean M_2 internal-tide SSH variance of the H12 simulation is about 40% ($\frac{0.035\ \text{cm}^2}{0.08\ \text{cm}^2}$) larger than the HYCOM simulation analyzed by Shriver et al. (2012) and Buijsman et al. (2016).

4.2.1. Mooring observations

Ansong et al. (2017) compare the simulated mode 1 and mode 2 M_2 internal tide energy fluxes to observed fluxes at 79 historical mooring locations. They find that the spatially-averaged mode-1 (mode-2) HYCOM fluxes, computed from model data subsampled at instrument depths, are 4% (32%) smaller than the observed fluxes, i.e γ equals 0.96 (0.68). The regression coefficient A is 0.82 (0.55). Luecke et al. (2020) compares KE and temperature variance in H25 for 3000 historical mooring observations. For the semidiurnal frequency band, γ is 0.64 and 0.44 and A is 0.64 and 0.47 for KE and temperature variance, respectively. In both studies, γ and A are close to unity, although the HYCOM values bias low, possibly due to the under-representation of higher modes in the simulations.

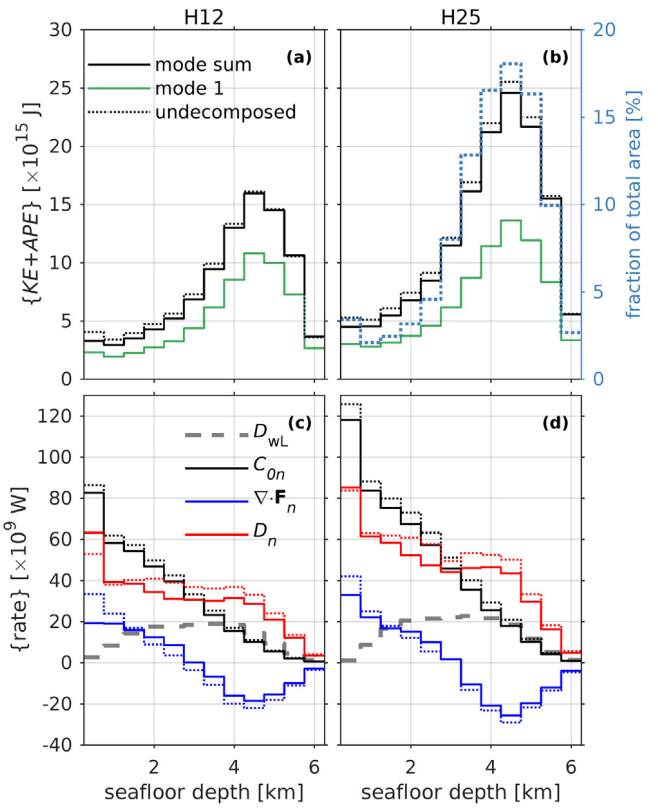

Fig. 13. Area- and depth-integrated (a and b) energy density and (c and d) terms from the baroclinic energy balance. The left column is for H12 and the right column for H25. All variables are area-integrated for 500-m seafloor depth bins from 250 to 6250 m. The dotted lines in (a–d) represent the undecomposed energy terms from Eq. (3) and the solid lines in (c–d) represent some of the energy terms from Eq. (9) summed over the first five modes. The blue dotted line and the right axis labels of (b) represent the fraction of the total area of 32.1×10^6 km^2.

4.2.2. Altimetry

How do these findings compare to the model validation of this paper? The corrected M_2 internal tide SSH variance of H25 for the one-year time series agrees well with altimetry after we apply a correction for time series duration ($r = 0.78$, $\gamma = 1.09$, and $A = 0.97$; Table 1 and Fig. 4). However, H25 is slightly more energetic than the altimetry; the corrected variance in the hotspot regions is 23% larger and the global-mean variance is 9% larger for the year-long time series. Despite this fair agreement, there are reasons for caution. First, we note that the correction factor represents both the nonstationary scattering and dissipation. It is not clear from this analysis how well HYCOM simulates the individual nonstationary scattering and dissipation processes. Moreover, the variance correction method also has some uncertainty: the corrected global-mean variances for the two-week and one-year long time series for H12 and H25 differ by about 20% ($\frac{0.018\ \text{cm}^2}{0.089\ \text{cm}^2}$) and 7% ($\frac{0.008\ \text{cm}^2}{0.112\ \text{cm}^2}$), respectively. Ideally, these differences should not exist after correction. Our correction method is based on the older HYCOM simulations discussed in Shriver et al. (2012) (Appendix). We do not yet know how the variance decay is affected by the higher horizontal and vertical resolution of the H12 and H25 simulations. On the other hand, there is uncertainty in separating the mesoscales from the internal tide scales in the altimetry signal (Ray and Byrne, 2010).

The differences between the corrected HYCOM and the altimetry-inferred fluxes for mode 1 and 2 are larger than for the SSH variance (Table 1 and Fig. 10), in particular for mode 2. Similar to the SSH variance, the predicted fluxes are larger than the altimetry fluxes. The differences may be attributed to the different flux calculation methods and the along-track bias of the plane-wave fit method.

The global integral of the resolved and parameterized surface to internal tide energy conversion ($\{C_L + D_{w0}\}$) for seafloor depths > 250 m in H25 is also in agreement with the surface tide dissipation inferred from TPXO8-atlas (Fig. 5). The dissipation in H25 is only 11% larger than in TPXO8-atlas. We are aware of several uncertainties associated with the calculation of D_{w0} in H25 and the surface tide dissipation inferred from TPXO8-atlas. The wave-drag dissipation in HYCOM should be computed using the total tidal flow: $D_w = \rho_c \mathbb{C} \mathbf{u}_t \cdot \mathbf{u}_t$ (Buijsman et al., 2016), where $\mathbb{C}$ is the wave drag and $\mathbf{u}_t = \mathbf{u} + \mathbf{U}$, $\mathbf{u}$, and $\mathbf{U}$ are the total, baroclinic, and barotropic horizontal velocity vectors, respectively. In order to avoid barotropic–baroclinic cross-terms based on $\mathbf{U}\cdot\mathbf{u}$, we apply a linear split to compute the barotropic and baroclinic components D_{w0} and D_{wL}. These terms are based on $\mathbf{u}_t \cdot \mathbf{U}$ and $\mathbf{u}_t \cdot \mathbf{u}$, respectively (Buijsman et al., 2016). We find that the cross-term amounts to about 10% of D_{w0}, which is about the same as the difference between $C_L + D_{w0}$ and TPXO. The surface tide dissipation from TPXO8-atlas has also some uncertainty. It is computed as a residual term. As a consequence, the dissipation as function of the horizontal coordinate has negative values at high latitudes and in some coastal shelf areas, where the TPXO solution is less-well constrained (Egbert and Ray, 2003; Green and Nycander, 2013; Buijsman et al., 2015). Egbert and Ray (2003) estimated error bars of 20% for an older TPXO inverse model.

4.2.3. Analytical conversion models

The modal conversion in the H25 simulation agrees very well with the analytical models by Falahat et al. (2014) and Vic et al. (2019) for seafloor depths > 700 m: the global integrals over the first 5 modes for the three models differ by less than 1% (Fig. 6b). We find that the mode-1 conversion for seafloor depths > 700 m constitutes about 21% ($\frac{0.19\ \text{TW}}{0.90\ \text{TW}}$) and 27% ($\frac{0.22\ \text{TW}}{0.83\ \text{TW}}$) of the sum of the resolved and parameterized conversion ($\sum_{n=1}^{5} C_{0n} + D_{w0}$) in H12 and H25, respectively. These ratios are in accordance with those computed with the analytical model by Vic et al. (2019): 34% and 29% when abyssal hills are excluded and included, respectively.

The catch is that a relatively large fraction of the resolved conversion in H25 occurs over seafloor depths ranging from 250 m to 750 m: about 21% of the conversion to modes 1–5 and about 31% of the conversion to mode 1. However, the shallow-water conversion rates of HYCOM are more difficult to validate because the analytical models break down on (super)critical slopes that mostly occur in shallow water.

Unfortunately, the 4-km HYCOM simulation and most other global simulations of similar and coarser resolution (see Introduction), the altimetry-constrained models, and the analytical conversion models are currently unable to reliably estimate the internal tide generation at shelf breaks and in shelf seas shallower than ~250 m at the global scale. Here thus lies an opportunity for future research to better constrain the barotropic to baroclinic conversion in these shallow seas.

4.2.4. Energy density

Few studies exist that report on estimates of the global internal tide energy. de Lavergne et al. (2019) computed 165 PJ in mode 1 for seafloor depths > 400 m. Zhao et al. (2016) applied a harmonic plane-wave fit to ~20-year long time series of altimetry SSH and estimated 36 PJ of energy in the mode-1 internal tide for seafloor depths greater than 500 m. The H25 mode-1 $\{KE + APE\}$ for seafloor depths > 500 m is 84.6 PJ, which is only 1.9% smaller than the energy for depths > 250 m (Fig. 9). Compared to H25 the mode-1 energy in the model of de Lavergne et al. (2019) is quite large. This may be attributed to the large wave–wave interaction e-folding decay times used in their model. The HYCOM and de Lavergne et al. (2019) internal-tide energy reflect the sum of the stationary and nonstationary fractions, whereas the altimetry-based estimate only reflects the stationary fraction. Moreover, Zhao et al. (2016) estimated energy by excluding the western

boundary and Antarctic Circumpolar current regions. Hence, we omit regions with $EKE > 200$ J m^{-2} for $|\phi| > 20°$ and we correct our mode-1 energy estimate of H25 with the spatially-varying correction factor from the Appendix. After these corrections, the globally integrated mode-1 stationary energy of H25 equals about 45 PJ, which is in closer agreement with the altimetry estimate by Zhao et al. (2016). As pointed out by de Lavergne et al. (2019), the estimate by Zhao et al. (2016) may still be a lower bound because the plane-wave fit technique is biased towards the north–south beams, which are more aligned with the altimetry tracks.

4.3. Future research

In contrast to Buijsman et al. (2016), de Lavergne et al. (2019), and Vic et al. (2019), we have not compared our HYCOM model simulations with microscale and finestructure dissipation observations in this paper. The nonlinear dissipation depends on the integral of all tidal flows, whereas we have only considered the M_2 tide in this paper. We plan to compute the dissipation due to the combined effect of the diurnal and semidiurnal internal tides and compare these with observations in a follow-up paper.

We have been fortunate with the choice of the wave drag set up in H25 as it provides accurate surface tides and it does not seem to greatly under- or overdamp the internal tides. These HYCOM experiments suggest that the need for an explicit baroclinic wave damping is mitigated in higher-resolution simulations because topographic wave scattering and wave–wave interactions are better resolved. Yet in our 4-km simulations some damping is still necessary. Ideally, we would like to apply an internal-tide damping term that is decoupled from the surface-tide damping. Most likely, such scheme would still need a tuning parameter.

5. Conclusions

In this paper we have performed a full and modal energy balance analysis for the M_2 internal tide in realistically-forced global HYCOM simulations with a horizontal resolution of 8 km (H12) and 4 km (H25). These simulations have been evaluated with altimetry inferred sea-surface height and fluxes, TPXO8-atlas surface tide dissipation rates, and analytical models of the barotropic to baroclinic energy conversion. Our most important findings are:

- The increase in horizontal grid size from 8 to 4 km coincides with a reduction in wave-drag strength by 40%. This reduction is due to the tuning of the drag to optimize the barotropic tidal accuracy. The associated reduction in surface tide energy loss to the wave drag, i.e. the parameterized energy conversion to the unresolved high modes, is offset by an increase in the barotropic to baroclinic energy conversion to the resolved baroclinic wave modes in H25. In both the H12 and H25 simulations, the sum of the resolved and parameterized conversion is equal, which is consistent with both simulations having the same tidal accuracy.
- The energy conversion is larger in H25 than in H12 because the higher resolution of H25 resolves up to 5 modes. In contrast, only 2 modes can be resolved in H12. For seafloor depths deeper than 250 m, the horizontal resolution, and not the vertical resolution, determines the number of modes that can be resolved, at least, in the simulations presented here.
- Overall, mode 1 is the dominant mode in both the H12 and H25 simulations. In both simulations, the mode-1 conversion constitutes about 30% of the sum of the resolved and parameterized conversion, which is in agreement with the analytical conversion model of Vic et al. (2019). In the H25 simulation, the mode-1 conversion is largest over the tall mid-ocean ridges and shelf breaks, whereas the higher-mode conversion becomes relatively more important over the deep mid-ocean ridges, such as the Mid-Atlantic Ridge.
- Compared to H12, the global integral of barotropic to baroclinic energy conversion in H25 has increased by 19% for mode 1 and by 49% for modes 1–5, while the global integral of the energy density has increased by 34% for mode 1 and by 60% for modes 1–5. The wave drag also dampens the internal tides. In a linear system, a 40% reduction in damping and a 19% increase in mode 1 conversion should double the mode-1 energy density when the grid size is increased from 8 to 4 km. However, the mode-1 energy density increase is much smaller because the increased resolution facilitates the transfer of energy out of mode 1 to smaller scales and higher frequencies due to enhanced topographic mode scattering (about 20% of the mode-1 conversion) and wave–wave interactions. The higher-resolution 4-km HYCOM simulation begins to cascade energy to smaller scales and higher frequencies, but these energy transfers are not yet strong enough to omit the application of an internal wave damping parameterization.
- H25 agrees better with observations and analytical models than H12 and a prior HYCOM simulation discussed in Buijsman et al. (2016). On the one hand, the comparison with the sparse mooring data suggests that H25 underestimates the internal tide energy by less than 10%, while on the other hand, the comparison with the altimetry-inferred SSH variance indicates that H25 overestimates the global-mean wave energy density by about 10% and the energy density in the hotspot regions by about 20%. The sum of the resolved and parameterized conversion in H25 is also 10% larger than the surface tide dissipation estimated from TPXO8-atlas. However, the simulated modal conversion rates are in good agreement with the analytical conversion models. It is plausible that these differences fall within the range of uncertainties associated with the analysis techniques and the validation data sets.
- The HYCOM and altimetry sea-surface height time series have durations of one year and about 20 years, respectively, which prevents a direct comparison of stationary tide signals. To permit an apples to apples comparison, we apply a correction to account for the decrease in the stationary signal as a function of the duration of a time series that includes both tidal and mesoscale variability (Appendix). This correction improves the correlation, regression, and variance ratios between the altimetry and corrected HYCOM data sets.

CRediT authorship contribution statement

Maarten C. Buijsman: Conceptualization, Formal analysis, Funding acquisition, Project administration, Visualization, Writing - original draft, Writing - review & editing. **Gordon R. Stephenson:** Formal analysis, Visualization, Writing - original draft, Writing - review & editing. **Joseph K. Ansong:** Writing - review & editing. **Brian K. Arbic:** Funding acquisition, Writing - review & editing. **J.A. Mattias Green:** Resources, Writing - review & editing. **James G. Richman:** Writing - review & editing. **Jay F. Shriver:** Formal analysis, Resources, Software, Writing - review & editing. **Clément Vic:** Resources, Writing - review & editing. **Alan J. Wallcraft:** Formal analysis, Resources, Software, Writing - review & editing. **Zhongxiang Zhao:** Resources, Writing - review & editing.

Declaration of competing interest

The authors declare that they have no known competing financial interests or personal relationships that could have appeared to influence the work reported in this paper.

Acknowledgments

M. Buijsman and G. Stephenson are funded by the Office of Naval Research (ONR), USA grants N00014-15-1-2288 and N00014-15-1-2578, National Science Foundation (NSF), USA grant OCE1537449,

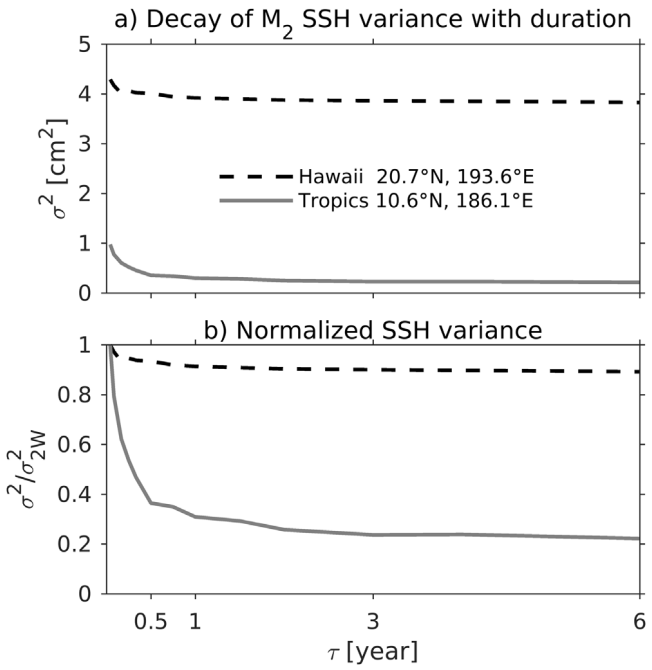

Fig. A.14. (a) M_2 internal-tide sea-surface height variance σ^2 as a function of time-series duration at a site near Hawaii with stationary internal tides and at a site in the central equatorial Pacific with nonstationary internal tides. (b) The variance normalized by the variance for a two-week long time series $\sigma^2{}_{2W}$.

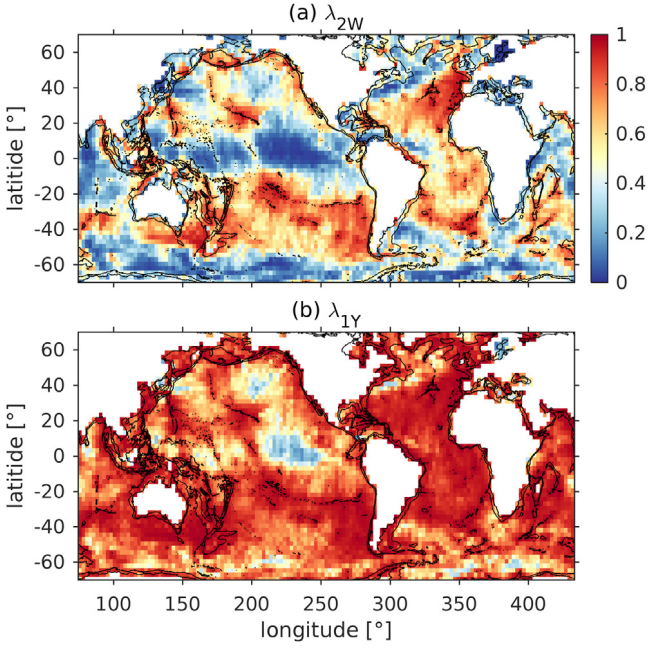

Fig. A.15. Correction factor λ_τ for a time-series that is (a) two weeks and (b) one-year long. The 0 and 2000 m seafloor depths are plotted as black contours.

and National Aeronautic Space Administration (NASA), USA grants 80NSSC18K0771 and NNX17AH55G. B.K. Arbic acknowledges support from ONR, USA grant N00014-15-1-2288, NASA grants NNX17AH55G and NNX16AH79G. J. Ansong and B. Arbic acknowledge funding from the University of Michigan, USA Associate Professor Support Fund, which is supported by the Margaret and Herman Sokol Faculty Awards, and from National Science Foundation (NSF), USA grant OCE-0968783; the latter was part of a multi-institution Climate Process Team grant, led by J. MacKinnon. We thank C. Whalen, A. Waterhouse, E. Kunze, and E. Zaron for comments and suggestions on an earlier version of this manuscript. Finally, we acknowledge the two reviewers who's comments and suggestions have improved this article.

Appendix. Computation of the variance correction factor

As internal tides propagate through a time-varying mesoscale background field, the observed Eulerian internal-tide amplitudes and phases will vary in time due to refraction, reflection, and ducting (Shriver et al., 2014; Zaron and Egbert, 2014; Zaron, 2017; Buijsman et al., 2017; Duda et al., 2018; Nelson et al., 2019). To extract amplitudes and phases (harmonic constants) from model simulations and observations, such as satellite altimetry and mooring records, a least-squares harmonic analysis is generally applied. This yields the stationary internal tide variance, which is inversely proportional to the duration of the time-series (Colosi and Munk, 2006; Nash et al., 2012; Ansong et al., 2015). In this paper, we validate two-week and one-year long M_2 steric sea-surface height (SSH) records of the HYCOM simulations with 17-year long altimetry records. M_2 SSH variance extracted from altimetry records that are longer than 10 years is most likely close to equilibrium, while HYCOM simulations of one year or shorter are not (Colosi and Munk, 2006; Ansong et al., 2015). Hence, we need to make a correction for the time-series duration to compare the stationary signal extracted from the HYCOM simulations with the stationary internal tide signal extracted from altimetry.

This correction factor has the form

$$\lambda_\tau = \frac{\sigma^2_{\mathrm{Oeq}}}{\sigma^2_{\mathrm{O}\tau}}, \tag{A.1}$$

where σ^2_{Oeq} is the equilibrium stationary variance and $\sigma^2_{\mathrm{O}\tau}$ is the stationary variance of a time-series with a duration τ. Both σ^2_{Oeq} and $\sigma^2_{\mathrm{O}\tau}$ can be spatially varying and should be computed from an observational record, e.g. altimetry, that is sufficiently long such that its variance has equilibrated. To compare the variance of the short-duration HYCOM simulations $\sigma^2_{\mathrm{H}\tau}$ with the equilibrated altimetry variance, the HYCOM variance can be corrected as follows

$$\sigma^2_{\mathrm{Heq}} = \lambda_\tau \sigma^2_{\mathrm{H}\tau}. \tag{A.2}$$

Technically, σ^2_{Oeq} and $\sigma^2_{\mathrm{O}\tau}$ should be computed from the altimetry record. However, the altimetry record is sparse with a sampling interval of ~10 days and no coverage poleward of 66°. The long sampling interval allows for the aliasing of non-tidal signals into the tidal record in the Western-Boundary current regions (Ray and Byrne, 2010) and makes it difficult to compute accurate $\sigma^2_{\mathrm{O}\tau}$ for time series records shorter than 3 to 4 years. Similar to Colosi and Munk (2006), we could use tide-gauge time series to compute λ_τ. However, the mesoscale background variability is variable in space (Shriver et al., 2014; Buijsman et al., 2017). Consequently, close to the internal tide generation site the internal tide is very stationary, while farther away from the source the nonstationary fraction is much larger. As is shown below, this also causes λ_τ to be spatially variable, in particular for time series shorter than one year.

To account for the spatial variability, we compute λ_τ using 8-km HYCOM simulations with a duration of six years. These simulations have been extensively discussed in Shriver et al. (2012), Buijsman et al. (2016), Ansong et al. (2015), and Nelson et al. (2019). Although the dynamics have improved in more recent HYCOM simulations (i.e. the 8 and 4-km simulations discussed in this paper) as compared to this six-year simulation, we argue that potentially adverse effects are mitigated by the fact that λ_τ is a ratio. For each horizontal grid point, we perform a least-squares fit to extract the M_2 stationary SSH variance $\sigma^2 = \frac{1}{2}|\tilde{\eta}|^2$, where $\tilde{\eta}$ is the complex harmonic constant. σ^2 is computed for τ equal

to 0.5, 1, 2, 3, 4, 6, and 9 months and 1, 1.5, 2, 3, 4, and 6 years. The time series with a duration of 2, 3, and 4 years have overlapping windows to compute better statistics. To reduce noise, we average the variance to 0.5° cells.

The decay of the M_2 stationary SSH variance as a function of time series duration is shown in Fig. A.14 for two locations along a beam radiating equatorward from Hawaii. One location near the source features relatively strong stationary tides and little variance decay. Here, the stationary fraction is 94% for a six-year time series duration. In contrast, the second location is in the equatorial Pacific, which features strong tropical instability wave variability (Buijsman et al., 2017). Hence, the variance decay is relatively strong and the stationary fraction is 21% for a time series duration of 6 years. The equilibrium variance at these two locations, as in most other places, is reached for durations of less than three years. For convenience, we assume that $\sigma^2_{\text{Oeq}} = \sigma^2_{\text{Heq}}$ and that equilibrium occurs for a duration of six years.

In this paper, we validate HYCOM sea-surface height and modal energetics computed for two-week and/or one-year long time series with altimetry. For this purpose the energetics and sea-surface height variance are corrected with λ_τ for two weeks and one year as shown in Fig. A.15a and b. λ_τ is largest near the generation sites and away from the equatorial jets and the Antarctic Circumpolar and Western Boundary currents. As the time-series duration increases from two weeks to one year, the correction factor becomes closer to unity (Fig. A.15b). However, in areas with strong mesoscale variability, like the Equatorial Pacific, λ_τ remains relatively small.

The identity $1 - \lambda_\tau$, where τ is equal to two weeks (Fig. A.15a), represents the ratio between the nonstationary M_2 variance and the total M_2 variance (nonstationary fraction) and is similar to maps of the nonstationary fraction in Figure 9 of Zaron (2017) and Figure 4 of Nelson et al. (2019). The globally averaged nonstationary fraction that we compute for the six-year long HYCOM time series is about 40%, which is similar to the 44% nonstationary fraction of Zaron (2017).

References

Adcroft, A., Hill, C., Marshall, J., 1999. A new treatment of the Coriolis terms in C-grid models at both high and low resolutions. Mon. Weather Rev. 127, 1928–1936.

Alford, M.H., Peacock, T., MacKinnon, J.A., Nash, J.D., Buijsman, M.C., Centuroni, L.R., Chao, S.Y., Chang, M.H., Farmer, D.M., Fringer, O.B., Fu, K.H., Gallacher, P.C., Graber, H.C., Helfrich, K.R., Jachec, S.M., Jackson, C.R., Klymak, J.M., Ko, D.S., Jan, S., Johnston, T.M.S., Legg, S., L, I.H., Lien, R.C., Mercier, M.J., Moum, J.N., Musgrave, R., Park, J.H., Pickering, A.I., Pinkel, R., Rainville, L., Ramp, S.R., Rudnick, D.L., Sarkar, S., Scotti, A., Simmons, H.L., St. Laurent, L.C., Venayagamoorthy, S.K., Wang, Y.H., Wang, J., Yang, Y.J., Paluszkiewicz, T., Tang, T.Y., 2015. The formation and fate of internal waves in the South China Sea. Nature 521, 65–69.

Ansong, J., Arbic, B., Alford, M., Buijsman, M., Shriver, J., Zhao, Z., Richman, J., Simmons, H., Timko, P., Wallcraft, A., Zamudio, L., 2017. Semidiurnal internal tide energy fluxes and their variability in a global ocean model and moored observations. J. Geophys. Res. 122, 1882–1900.

Ansong, J., Arbic, B., Buijsman, M., Richman, J., Shriver, J., Wallcraft, A., 2015. Indirect evidence for substantial damping of low-mode internal tides in the open ocean. J. Geophys. Res. 120, 6057–6071.

Ansong, J., Arbic, B., Simmons, H., Alford, M., Buijsman, M., Timko, P., Richman, J., Shriver, J., Wallcraft, A., 2018. Geographical distribution of diurnal and semidiurnal parametric subharmonic instability in a global ocean circulation model. J. Phys. Oceanogr. 48, 1409–1431.

Arakawa, A., Lamb, V.R., 1977. Computational design of the basic dynamical processes of the UCLA general circulation model. In: Chang, J. (Ed.), Methods in Computational Physics. Academic Press, pp. 174–267.

Arbic, B., Alford, M., Ansong, J., Buijsman, M., Ciotti, R., Farrar, J., Hallberg, R., Henze, C., Hill, C., Luecke, C., Menemenlis, D., Metzger, E.J., Müller, M., Nelson, A., Nelson, B., Ngodock, H., Ponte, R., Richman, J., Savage, A., Scott, R., Shriver, J., Simmons, H., Souopgui, I., Timko, P., Wallcraft, A., Zamudio, L., Zhao, Z., 2018. A primer on global internal tide and internal gravity wave continuum modeling in HYCOM and MITgcm. In: Chassignet, E., Pascual, A., Tintore, J., Verron, J. (Eds.), New Frontiers in Operational Oceanography. GODAE OceanView, pp. 307–392.

Arbic, B.K., Garner, S.T., Hallberg, R.W., Simmons, H.L., 2004. The accuracy of surface elevations in forward global barotropic and baroclinic tide models. Deep-Sea Res. II 51, 3069–3101.

Arbic, B.K., Wallcraft, A.J., Metzger, E.J., 2010. Concurrent simulation of the eddying general circulation and tides in a global ocean model. Ocean Modell. 32, 175–187.

Bell, T.H., 1975. Topographically generated internal waves in the open ocean. J. Geophys. Res. 80, 320–327.

Buijsman, M., Ansong, J., Arbic, B., Richman, J., Shriver, J., Timko, P., Wallcraft, A., Whalen, C., Zhao, Z., 2016. Impact of parameterized internal wave drag on the semidiurnal energy balance in a global ocean circulation model. J. Phys. Oceanogr. 46, 1399–1419.

Buijsman, M.C., Arbic, B.K., Green, J.A.M., Helber, R.W., Richman, J.G., Shriver, J.F., Timko, P.G., Wallcraft, A.J., 2015. Optimizing internal wave drag in a forward barotropic model with semidiurnal tides. Ocean Modell. 85, 42–55.

Buijsman, M., Arbic, B., Kelly, S., Waterhouse, A., 2019. Internal gravity waves. In: Cochran, J., Bokuniewicz, H., Yager, P. (Eds.), Encyclopedia of Ocean Sciences, third ed. Academic Press, pp. 622–632.

Buijsman, M.C., Arbic, B.K., Richman, J.G., Shriver, J.F., Wallcraft, A.J., Zamudio, L., 2017. Semidiurnal internal tide incoherence in the equatorial Pacific. J. Geophys. Res. 122, 5286–5305.

Buijsman, M.C., Jackson, C., McWilliams, J.C., 2010. East-west asymmetry in nonlinear internal waves from Luzon Strait. J. Geophys. Res. 115.

Buijsman, M., Klymak, J., Legg, S., Alford, M., Farmer, D., MacKinnon, J., Nash, J., Park, J.H., Pickering, A., Simmons, H., 2014. Three-dimensional double-ridge internal tide resonance in Luzon Strait. J. Phys. Oceanogr. 44, 850–869.

Buijsman, M.C., Legg, S., Klymak, J., 2012. Double ridge internal tide interference and its effect on dissipation in Luzon Strait. J. Phys. Oceanogr. 42, 1337–1356.

Colosi, J., Munk, W., 2006. Tales of the venerable Honolulu tide gauge. J. Phys. Oceanogr. 36, 967–996.

Duda, T., Lin, Y., Buijsman, M., Newhall, A., 2018. Internal tidal modal ray refraction and energy ducting in baroclinic Gulf Stream currents. J. Phys. Oceanogr. 48, 1969–1993.

Eden, C., Olbers, D., 2014. An energy compartment model for propagation, nonlinear interaction, and dissipation of internal gravity waves. J. Phys. Oceanogr. 44, 2093–2106.

Egbert, G.D., Bennett, A.F., Foreman, M.G.G., 1994. TOPEX/POSEIDON tides estimated using a global inverse model. J. Geophys. Res. 99, 24821–24852.

Egbert, G.D., Ray, R.D., 2003. Semi-diurnal and diurnal tidal dissipation from TOPEX/Poseidon altimetry. Geophys. Res. Lett. 30.

Falahat, S., Nycander, J., Roquet, F., Zarroug, M., 2014. Global calculation of tidal energy conversion into vertical normal modes. J. Phys. Oceanogr. 44, 3225–3244.

Fu, L.L., Alsdorf, D., Morrow, R., Rodrigues, E., Mognard, N., 2012. SWOT: The Surface Water and Ocean Topography Mission - wide-swath altimetric measurement of water elevation on Earth. JPL Publ. 12 (5).

Gerkema, T., Zimmerman, J.T.F., 2008. An Introduction to Internal Waves. In: Lecture Notes, Royal Netherlands Institute for Sea Research.

Green, J.A.M., Nycander, J., 2013. A comparison of tidal conversion parameterizations for tidal models. J. Phys. Oceanogr. 43, 104–119.

Hallberg, R., 2005. A thermobaric instability of Lagrangian vertical coordinate ocean models. Ocean Model. 8, 279–300.

Hogan, T., Liu, M., Ridout, J., Peng, M., Whitcomb, T., Ruston, B., Reynolds, C., Eckermann, S., Moskaitis, J., Baker, N.L., McCormack, J., Viner, K., McLay, J., Flatau, M., Xu, L., Chen, C., Chang, S., 2014. The navy global environmental model. Oceanography 27, 116–125.

Jayne, S.R., St. Laurent, L.C., 2001. Parameterizing tidal dissipation over rough topography. Geophys. Res. Lett. 28, 811–814.

Johnston, T.M.S., Merrifield, M.A., Holloway, P.E., 2003. Internal tide scattering at the Line Islands Ridge. J. Geophys. Res. 108 (C11).

Jungclaus, J.H., Botzet, M., Haak, H., Keenlyside, N., Luo, J.J., Latif, M., Marotzke, J., Mikolajewicz, U., Roeckner, E., 2006. Ocean circulation and tropical variability in the coupled model ECHAM5/MPI-OM. J. Climate 19, 3952–3972.

Kelly, S.M., Nash, J.D., 2010. Internal-tide generation and destruction by shoaling internal tides. Geophys. Res. Lett. 37.

Kelly, S.M., Nash, J.D., Martini, K.I., Alford, M.H., Kunze, E., 2012. The cascade of tidal energy from low to high modes on a continental slope. J. Phys. Oceanogr. 42, 1217–1232.

Kerry, C., Powell, B., Carter, G., 2013. Effects of remote generation sites on model estimates of M2 internal tides in the Philippine Sea. J. Phys. Oceanogr. 43, 187–204.

Kunze, E., 2017. Internal-wave-driven mixing: global geography and budgets. J. Phys. Oceanogr. 47, 1325–1345.

de Lavergne, C., Falahat, S., Madec, G., Roquet, F., Nycander, J., Vic, C., 2019. Toward global maps of internal tide energy sinks. Ocean Modell. 137, 52–75.

Legg, S., Huijts, K.M.H., 2006. Preliminary simulations of internal waves and mixing generated by finite amplitude tidal flow over isolated topography. Deep-Sea Res. II 53, 140–156.

Luecke, C., Arbic, B., Richman, J., Shriver, J., Alford, M.H., Ansong, J., Bassette, S., Buijsman, M., Menemenlis, D., Scott, R., Timko, P., Voet, G., Wallcraft, A., Zamudio, L., 2020. Statistical comparisons of temperature variance and kinetic energy in global ocean models and observations: results from mesoscale to internal wave frequencies. J. Geophys. Res. 125, e2019JC015306.

MacKinnon, J., Zhao, Z., Whalen, C., Waterhouse, A., Trossman, D., Sun, O., St. Laurent, L., Simmons, H., Polzin, K., Pinkel, R., Pickering, A., Norton, N., Nash, J., Musgrave, R., Merchant, L., Melet, A., Mater, B., Legg, S., Large, W., Kunze, E., Klymak, J., Jochum, M., Jayne, S., Hallberg, R., Griffies, S., Diggs, S., Danabasoglu, G., Chassignet, E., Buijsman, M., Bryan, F., Briegleb, B., Barna, A., Arbic, B., Ansong, J., Alford, M., 2017. Climate process team on internal wave–driven ocean mixing. Bull. Amer. Meteor. Soc. 98, 2429–2454.

Marshall, J., Adcroft, A., Hill, C., Perelman, L., Heisey, C., 1997. A finite-volume, incompressible Navier Stokes model for studies of the ocean on parallel computers. J. Geophys. Res. 102, 5753–5766.

Mazloff, M.R., Cornuelle, B., Gille, S.T., Wang, J., 2020. The importance of remote forcing for regional modeling of internal waves. J. Geophys. Res. 125, e2019JC015623.

Melet, A., Hallberg, R., Legg, S., Polzin, K., 2013. Sensitivity of the ocean state to the vertical distribution of internal-tide-driven mixing. J. Phys. Oceanogr. 43, 602–615.

Metzger, E., Smedstad, O., Thoppil, P., Hurlburt, H., Cummings, J., Wallcraft, A., Zamudio, L., Franklin, D., Posey, P., Phelps, M., Hogan, P., Bub, F., DeHaan, C., 2014. US navy operational global ocean and arctic ice prediction systems. Oceanography 27, 32–43.

Müller, M., Arbic, B., Richman, J., Shriver, J., Kunze, E., Scott, R., Wallcraft, A., Zamudio, L., 2015. Toward an internal gravity wave spectrum in global ocean models. Geophys. Res. Lett. 42, 3474–3481.

Müller, M., Cherniawsky, J., Foreman, M., von Storch, J.S., 2012. Global map of M_2 internal tide and its seasonal variability from high resolution ocean circulation and tide modelling. Geophys. Res. Lett. 39.

Munk, W., Wunsch, C., 1998. Abyssal Recipes II: energetics of tidal and wind mixing. Deep-Sea Res. 45, 1977–2010.

Nash, J., Shroyer, E., Kelly, S., Inall, M., Duda, T., Levine, M., Jones, N., Musgrave, R., 2012. Are any coastal internal tides predictable? Oceanography 25, 80–95.

Nelson, A., Arbic, B., Zaron, E., Savage, A., Richman, J., Buijsman, M., Shriver, J., 2019. Toward realistic nonstationarity of semidiurnal baroclinic tides in a hydrodynamic model. J. Geophys. Res. 124, 6632–6642.

Ngodock, H.E., Souopgui, I., Wallcraft, A.J., Richman, J.G., Shriver, J.F., Arbic, B.K., 2016. On improving the accuracy of the M_2 barotropic tides embedded in a high-resolution global ocean circulation model. Ocean Modell. 97, 16–26.

Niwa, Y., Hibiya, T., 2014. Generation of baroclinic tide energy in a global three-dimensional numerical model with different spatial grid resolutions. Ocean Modell. 80, 59–73.

Ponte, A., Cornuelle, B., 2013. Coastal numerical modelling of tides: Sensitivity to domain size and remotely generated internal tide. Ocean Modell. 62, 17–26.

Rainville, L., Pinkel, R., 2006. Propagation of low-mode internal waves through the ocean. J. Phys. Oceanogr. 36, 1220–1236.

Ray, R., Byrne, D., 2010. Bottom pressure tides along a line in the southeast Atlantic Ocean and comparisons with satellite altimetry. Ocean Dynam. 60, 1167–1176.

Ray, R., Zaron, E., 2016. M_2 internal tides and their observed wavenumber spectra from satellite altimetry. J. Phys. Oceanogr. 46, 3–22.

Savage, A., Arbic, B., Alford, M., Ansong, J., Farrar, J., Menemenlis, D., O'Rourke, A., Richman, J., Shriver, J., Voet, G., Wallcraft, A., Zamudio, L., 2017a. Spectral decomposition of internal gravity wave sea surface height in global models. J. Geophys. Res. 119, 7803–7821.

Savage, A., Arbic, B., Richman, J., Shriver, J., Alford, M., Buijsman, M., Farrar, J., Sharma, H., Voet, G., Wallcraft, A., Zamudio, L., 2017b. Frequency content of sea surface height variability from internal gravity waves to mesoscale eddies. J. Geophys. Res. 122.

Shriver, J.F., Arbic, B.K., Richman, J.G., Ray, R.D., Metzger, E.J., Wallcraft, A.J., Timko, P.G., 2012. An evaluation of the barotropic and internal tides in a high resolution global ocean circulation model. J. Geophys. Res. 117.

Shriver, J.F., Richman, J.G., Arbic, B.K., 2014. How stationary are the internal tides in a high-resolution global ocean circulation model? J. Geophys. Res. 119.

Simmons, H.L., Hallberg, R.W., Arbic, B.K., 2004. Internal wave generation in a global baroclinic tide model. Deep-Sea Res. II 51, 3043–3068.

Vic, C., Naveira-Garabato, A., Green, J., Waterhouse, A., Zhao, Z., Melet, A., de Lavergne, C., Buijsman, M., Stephenson, G., 2019. Deep-ocean mixing driven by small-scale internal tides. Nature Commun. 10 (2099).

Waterhouse, A., MacKinnon, J., Nash, J., Alford, M., Kunze, E., Simmons, H., Polzin, K., St. Laurent, L., Sun, O., Pinkel, R., Talley, L., Whalen, C.B., Huussen, T., Carter, G., Fer, I., Waterman, S., Garabato, A.N., Sanford, T., Lee, C., 2014. Global patterns of diapycnal mixing from measurements of the turbulent dissipation rate. J. Phys. Oceanogr. 44, 1854–1872.

Whalen, C.B., Talley, L.D., MacKinnon, J.A., 2012. Spatial and temporal variability of global ocean mixing inferred from Argo profiles. Geophys. Res. Lett. 39.

Wunsch, C., Ferrari, R., 2004. Vertical mixing, energy, and the general circulation of the oceans. Annu. Rev. Fluid Mech. 281–314.

Yu, X., Ponte, A.L., Elipot, S., Menemenlis, D., Zaron, E.D., Abernathey, R., 2019. Surface kinetic energy distributions in the global oceans from a high-resolution numerical model and surface drifter observations. Geophys. Res. Lett. 46, 9757–9766.

Zaron, E.D., 2017. Mapping the nonstationary internal tide with satellite altimetry. J. Geophys. Res. Oceans 122, 539–554.

Zaron, E.D., Egbert, G.D., 2014. Time-variable refraction of the internal tide at the Hawaiian Ridge. J. Phys. Oceanogr. 44, 538–557.

Zhao, Z., 2018. The global mode-2 M2 internal tide. J. Geophys. Res. 123, 7725–7746.

Zhao, Z., Alford, M., Girton, J., Rainville, L., Simmons, H., 2016. Global observations of open-ocean mode-1 M_2 internal tides. J. Phys. Oceanogr. 46, 1657–1684.